



저작자표시-비영리-변경금지 2.0 대한민국

이용자는 아래의 조건을 따르는 경우에 한하여 자유롭게

- 이 저작물을 복제, 배포, 전송, 전시, 공연 및 방송할 수 있습니다.

다음과 같은 조건을 따라야 합니다:



저작자표시. 귀하는 원저작자를 표시하여야 합니다.



비영리. 귀하는 이 저작물을 영리 목적으로 이용할 수 없습니다.



변경금지. 귀하는 이 저작물을 개작, 변형 또는 가공할 수 없습니다.

- 귀하는, 이 저작물의 재이용이나 배포의 경우, 이 저작물에 적용된 이용허락조건을 명확하게 나타내어야 합니다.
- 저작권자로부터 별도의 허가를 받으면 이러한 조건들은 적용되지 않습니다.

저작권법에 따른 이용자의 권리는 위의 내용에 의하여 영향을 받지 않습니다.

이것은 [이용허락규약\(Legal Code\)](#)을 이해하기 쉽게 요약한 것입니다.

[Disclaimer](#)

공학박사 학위논문

**Evaluation of Impact Property through Analysis of
Dynamic Deformation during Indentation Impact
Test of Metallic Materials**

압입충격시험의 동적 변형거동 해석을 통한
재료의 충격특성평가

2016년 2월

서울대학교 대학원

재료공학부

조원제

Evaluation of Impact Property through Analysis of Dynamic Deformation during Indentation Impact Test of Metallic Materials

압입충격시험의 동적 변형거동 해석을 통한
재료의 충격특성평가

지도교수 권 동 일

이 논문을 공학박사 학위논문으로 제출함
2015년 12월

서울대학교 대학원
재료공학부
조 원 제

조원제의 박사학위논문을 인준함
2015년 12월

위원장	한홍남	(인)
부위원장	권동일	(인)
위원	선정운	(인)
위원	길학민	(인)
위원	김우식	(인)

Abstract

Jo, Won Je

Dept. Materials Science and Engineering

The Graduate School

Seoul National University

The safety and reliability assessment of structural components is important because seemingly minor flaws can cause extensive damage to or total failure of the system. Damage initiated by small breakages in huge systems such as heavy industries, power plants or nuclear facilities may occasion large economic costs and also hazard to human life. In particular, extreme service conditions for structural components can reduce performance and lessen lifetime. Thus, understanding the performance of structural components under such conditions is of major importance in assessing total system service. However, measuring the properties of in-use materials is not easy because conventional mechanical tests are difficult to apply in the field. In = nuclear power plants, the primary mechanical fracture performance for safety assessment is generally defined as Charpy V-notch impact testing (CVN testing). However, CVN testing of in-field structural components is

severely limited because the CVN testing process includes fracture of the specimen.

Thus, instrumented indentation testing (IIT) can be a reasonable method for measuring mechanical properties of in-field facilities because it requires neither specific sample dimensions nor large samples. Also, it offers the advantage that measuring localized properties can make it easier to find weak points by property mapping.

Because of these advantages, many attempts have been made to assess the fracture performance of structural components through indentation testing. However, correlating the generally used fracture performance in CVN tests with indentation properties is difficult because indentation results are defined from static deformation behavior while the CVN test is based on dynamic deformation behavior. Additional strain rate theories must be considered to overcome these limitations. Here a solution is suggested: a technique for indentation testing under dynamic conditions called *indentation impact testing*.

The present study focuses on absorbed energy because CVN test results are given in energy terms. Determination of the absorbed indentation impact energy corresponding to CVN energy is proposed based on similarities in geometry, stress distribution, and crack history in CVN testing and indentation impact testing. And the corresponding indentation impact energy

is interpreted in terms of stages of indentation crack formation (flaw initiation, crack enlargement, crack propagation) using strain rate criteria that are estimated from the change in plastic zone expansion rate and definition of the indentation strain rate.

The values of indentation impact energy were estimated for more than 14 different metallic materials and compared with the values from standard Charpy V-notch impact tests. The results showed good agreement between the two methods (within $\pm 20\%$ error range) and displayed very similar tendency. These results showed that indentation impact testing is effective in inspection of in-service structural components to monitor the CVN energy variation in materials due to degradation. Also, this test can be suggested an alternative method to Charpy V-notch impact testing when the components are restricted in various ways, e.g., small-size specimen or limited region available for testing.

Keywords: Indentation impact test; CVN impact energy; Indentation crack formation; Strain rate change criterion

Student Number: 2009-20639

Contents

Abstract	3
Contents	6
List of Tables	8
List of Figures	9
Chapter 1. Introduction	15
1.1. Objective and Scope of This Study	16
1.2. Outline of the Thesis	21
Chapter 2. Research Background	23
2.1. Fracture Mechanics in Impact Fracture	24
2.1.1. The Energy Criterion	
2.1.2. Qualitative Toughness Tests	
2.1.3. Historical Review of Impact Testing	
2.2. The Instrumented Indentation Technique	32
2.2.1. Introduction to the Instrumented Indentation Technique	
2.2.2. Application of the Instrumented Indentation Technique	
2.2.3. Indentation Crack Formation with Sharp Indenter	
2.2.4. Dynamic Indentation Technique	
Chapter 3. Strain-Rate-Dependent Indentation Fracture Characteristics	62
3.1. Influence of Strain Rate on Indentation Fracture Characteristics	63
Chapter 4. Theoretical Modeling of Indentation Impact Energy	73
4.1. Development of Indentation Impact Energy Model	74
4.1.1. Introduction	
4.1.2. Indentation Impact Energy Model	
Chapter 5. Model Verification	112
5.1. Experimental Details	113

5.2. Results and Discussion	119
5.2.1. Determination of Indentation Impact Energy	
5.2.2. Comparison of CVN Energy Measured from Indentation Impact and CVN Tests	
Chapter 6. Conclusions	125
References	130
Appendix A. Model Extension	137
Abstract in Korean	146
List of Publications	149
Acknowledgments in Korean	152

List of Tables

Table 3.1.

In-situ nanoindentation results at various strain rates.

Table 5.1

List of materials tested.

List of Figures

Figure 2.1.

Schematic diagram of typical load-depth curve during instrumented indentation.

Figure 2.2.

Cross section of contact morphology in the loaded state and residual indent by a sharp indenter after unloading.

Figure 2.3.

Variation in indentation loading curves with changes in stress state.

Figure 2.4.

Theoretical surface morphologies around the contact for (a) stress-free, (b) tensile stress, and (c) compressive stress states.

Figure 2.5.

Crack system for Vickers indenter: (a) radial cracks, (b) lateral cracks, (c) median cracks, and (d) half-penny cracks.

Figure 2.6.

Schematic of radial cracking by Vickers indentation.

Figure 2.7.

Crack formation process during sharp indentation.

Figure 2.8.

Nucleation of indentation-induced flaw from stress concentration due to dislocation pile-up at slip band intersect [65].

Figure 2.9.

Strain rate regimes of current test devices [99].

Figure 2.10.

NanoTest Vantage (Micro Materials).

Figure 3.1.

In-situ SEM nanoindentation.

Figure 3.2.

SEM image of frit-bonding specimen.

Figure 3.3.

Crack-like morphology within indented surface: (a), (b) V-P-based frit bonding, (c) Bi-based frit bonding. (d) Schematic of crack-like morphology.

Figure 3.4.

Indentation (a) hardness and (b) elastic modulus at various strain rates.

Figure 3.5.

E/H ratio at various strain rates.

Figure 4.1.

Distribution of radial stress of indentation along the z-axis.

Figure 4.2.

Schematic longitudinal stress distribution ahead of a rounded notch at general yielding: rigid plastic slip-line field solution.

Figure 4.3.

TEM analysis of indentation-induced flaw formation from cross-sectional nanoindentation trace [100].

Figure 4.4.

Schematic of an ideal vent crack formation beneath point load indentation. Fracture starts from inelastic deformation (dark zone) [29].

Figure 4.5.

Indentation-induced pile-up trace in indentation impact test.

Figure 4.6.

Crack-like feature of Vickers indentation impact trace.

Figure 4.7.

Strain rate change during impact loading of indentation impact containing crack formation steps.

Figure 4.8.

Difference in absorbed energy during crack propagation due to specimen failure in CVN test.

Figure 4.9.

Relation between CVN energy and indentation impact energy due to assumed similarities: linear relation of (a) absorbed energy and (b) rate of absorbed energy increase.

Figure 4.10.

Constant rate of absorbed energy increase of indentation impact during crack propagation.

Figure 4.11.

Iteration for constant K compensation.

Figure 4.12.

FEA simulation of CVN test using ANSYS.

Figure 4.13.

Change in load-displacement curve with material ductility.

Figure 4.14.

Estimate of crack initiation energy criterion based on ductility criterion of CVN energy from transition temperatures [64].

Figure 4.15.

Steps in indentation impact energy model with ductility criterion.

Figure 5.1.

Indentation impact system.

Figure 5.2.

Sharp indentation impact loading curve and typical indentation curve.

Figure 5.3.

Geometry of CVN specimen used in CVN test (ASTM E specifications).

Figure 5.4.

Equipment and specimen for CVN tests.

Figure 5.5.

Indentation impact energy (J) vs. CVN energy (J).

Figure 5.6.

CVN energy (J) estimated from indentation impact energy vs. CVN energy (J) in reference test.

Figure 5.7.

Transition behavior of (a) SA508 and (b) tempered SA508 from CVN energy change from CVN test and indentation impact test.

Figure A.1.

Basic concept of indentation impact test system.

Figure A.2.

Solenoid actuator (LH0600008).

Figure A.3.

Laser displacement sensor (HL-C201A).

Figure A.4.

Dynamic load cell (CSBA).

Figure A.5.

Indentation impact test system.

Figure A.6.

Scattered raw data for impact displacement vs. time.

Figure A.7.

Logistic curve fitting of indentation impact load vs. time curve.

Symbols and Notation

Symbol	Designation
t_{pc}	Crack propagation time in CVN impact test
t_1	Crack initiation time in indentation impact test
t_2	Crack propagation start time in indentation impact test
t_e	End time of test
t_i	True crack propagation end time of indentation impact test
t_{pe}	= $t_e - t_2$: crack propagation time until test ends
t_{pi}	= $t_i - t_2$: true crack propagation time in indentation impact test
h_{t1}	Displacement at t_1
h_{t2}	Displacement at t_2
h_{te}	Displacement at end of test
h_{ti}	Displacement at true propagation end time
CVN_I	CVN crack initiation energy
CVN_E	CVN crack enlargement energy
CVN_P	CVN crack propagation energy
E_i	Indentation impact energy
E_{li}	Indentation impact crack initiation energy
E_{Ei}	Indentation impact crack enlargement energy
E_{Pi}	Indentation impact crack propagation energy
E_{Pe}	Indentation impact crack propagation energy until end of test
K	Ratio of energy: CVN and indentation impact energy
S	Ratio of crack propagation energy increase rates

Chapter 1

INTRODUCTION

Contents

1.1. Objective and Scope of This Study	16
.....	
1.2. Outline of the Thesis	21
.....	

1.1 Objective and Scope of This Study

Safety assessment of in-service components is one of the most important considerations in industrial structural integrity because service conditions can induce far worse performance and shorter lifetime than was designed. Since small flaws can cause extensive systems damage or indeed total failure, the in-service performance of such huge systems as power plants or nuclear facilities, which can be hazardous to human life and economic well-being, must be considered for structural integrity. Fitness for Service (FFS) is a quantitative engineering evaluation that demonstrates the structural integrity of an in-service component. In FFS assessment, three facts are considered: the appropriate applied stress for the given application, acceptable flaw size and shape, and appropriate material properties.

Applied stresses are considered designed stresses and information on acceptable flaws can be determined by non-destructive techniques. However, the ability to determine the appropriate material properties of in-service components can be limited with conventional test methods, such as tensile tests or fracture tests, due to their low in-field applicability. Thus a method that can be used for in-service material property testing is highly desirable.

Among the issues required for safety assessment of in-service components, fracture performance is one of the most important. For nuclear power plants,

the primary mechanical fracture performance in safety assessment is defined from Charpy V-notch impact testing (CVN testing). The CVN test has many advantages due to simple and easy test procedure. Though the CVN test result is defined as an energy term, CVN energy, it is regarded as a basic method to derive a material's fracture property. The test details are standardized in ASTM E23 [3]. CVN testing is widely used to verify a material's ductile-to-brittle transition behavior from the different values of CVN energy with fracture behavior. Transition temperature, RT_{NDT} , is defined by the transition behavior of CVN energy with temperature change. RT_{NDT} from the CVN test is used as a reliability criterion for uncertainty in ductile-to-brittle transition behavior induced by external conditions such as embrittlement.

It is clear that fracture toughness has a close relationship with CVN energy. Due to the difficulty of fracture toughness testing, many researchers have worked to derive a modeling between CVN energy and fracture toughness [64]. However, CVN testing requires more than certain amount of specimens of standardized dimensions. Thus the use of CVN testing on in-field structural components has severe limitations.

The instrumented indentation test (IIT) is a candidate method for evaluating fracture performance (CVN energy) in in-field components because of its simple test procedure. Also, it does not require specific sample

dimensions since it measures a localized property. The IIT test could make possible lifetime monitoring of real structures with little or no sample preparation and merely localized testing. As indentation testing is performed by a static deformation process, however, measuring CVN energy directly from indentation results is severely restricted.

Thus attempts to defining fracture performance with fracture toughness have been made by many researchers. However, in addition to its various attractions, estimation of fracture toughness from instrumented indentation tests also has many restrictions. Most researchers have focused on the relation between crack length and indentation load and fracture toughness (K_{IC}) based on indentation crack formation. Palmquist [28], recognizing that the indentation-induced cracking observed on cermets was related to fracture toughness, developed a procedure for predicting fracture toughness. Lawn and Wilshaw [29] predicted fracture toughness with formation of fully developed cone crack in soda-lime glass under spherical indentation. The formation of crack is based on researches below. Lawn and Swain [30], using linear elastic fracture mechanics, showed that for soda-lime glass and a Vickers indenter, a median vent crack length extends stably in proportion to the load. Lawn and Fuller [31] observed crack formation of sharp Vickers diamond-pyramid indenters of Vickers and conical indenters with half-cone angles from 30° to 80° in 10° intervals. However, in metallic materials

indentation cracking does not occur easily; previous indentation-based theories and models are restricted to brittle materials only.

Another approach to fracture performance evaluation in IIT focuses on fracture behavior in dynamically deformed indentation tests. Dynamic deformation is induced by increasing the loading rate of the indentation test device. As the dynamic indentation test process is performed with dynamic deformation process, a direct relation to CVN energy is more reasonable. Most approaches of dynamic indentation are based on the concept of dynamic hardness which is known to have close relationship with dynamic fracture performance. Martel [79] first recognized the concept of rate-dependent hardness and Batson [70] and Yoshioka and Naoto [86] developed the rebound method, a way to evaluate hardness with dynamic strain rate (previous methods define hardness by an energy change and do not measure indentation load directly). Tabor [87] expanded the concept of dynamic hardness to IIT hardness, which is defined with normalized energy with deformed volume. Tabor's concept of indentation dynamic hardness focuses on the trend in indentation hardness change with increasing strain rate. Koeppel and Subhash [76] insisted the indentation dynamic hardness with standard hardness test method of Vickers hardness. Chaudhri [89] explained dynamic hardness by indentation crack formation of ionic crystals.

Though CVN energy trends can be predicted by previous dynamic

hardness results, more information on the fracture process must be included to estimate fracture performance directly. Jennett suggests [94] measuring indentation impact energy with indentation-induced fracture of fused silica. Jennett focused on the change in the dynamic indentation curve with the indentation-induced fracture. However, these attempts are still restricted to brittle materials and test results are derived from the concept of kinetic energy (calculated from the velocity change), giving rise to many errors in detection.

This previous work makes it clear that estimation of the fracture performance (CVN energy) using an indentation-based method must overcome 1) indentation-induced cracking in metallic materials, 2) indentation fracture with dynamic deformation, and 3) errors in detection.

The present work uses a dynamic indentation method with strain rates up to 10^3 and exploits the concept of indentation impact energy to estimate fracture performance (CVN energy) in metallic materials. Indentation-induced cracking in metallic materials is subsumed within the concept of enlarged work-hardening behavior during dynamic deformation. Indentation fracture with dynamic deformation is explained using Johanns' [60] indentation cracking process. Indentation fracture during dynamic deformation is analyzed from the indentation impact load-displacement curve with a criterion derived from Johnson's [58] expanding rate of plastic

deformation change during indentation crack formation.

The indentation impact energy corresponding to CVN energy is defined by analysis of the indentation impact load-displacement curve from the proposed model. The proposed model was verified in the laboratory and then applied in two practical areas: 1) the variation of CVN energy at low temperatures and 2) on-site testing of tempered embrittlement.

1.2 Outline of the Thesis

This thesis has six parts. After a brief introduction in Chapter 1, Chapter 2 gives a historical overview of fracture mechanics in impact fracture and methods for measuring absorbed impact fracture energy. Chapter 2 also gives a detailed description of the instrumented indentation technique and the basic principles of instrumented indentation tests (IIT), a nondestructive technique for evaluating mechanical properties such as hardness, elastic modulus, tensile properties, residual stress, fracture toughness, and the like.

Theories of and methods for IIT are discussed in detail, in particular previous work on indentation crack formation and dynamic indentation properties. Strain rate dependency of indentation fracture characteristics is discussed in Chapter 3 within the domain of nanoscale dynamic indentation. Theoretical models for estimating CVN energy are presented in Chapter 4. In

Chapter 5, laboratory work to verify the proposed model is described and the results are discussed. Finally, conclusions and extensions of the model to low temperatures and to the measurement of tempered embrittlement are given.

Chapter 2

RESEARCH BACKGROUND

Contents

2.1	Fracture Mechanics in Impact Fracture	24
	
	2.1.1. The Energy Criterion	
	2.1.2. Qualitative Toughness Tests	
	2.1.3. Historical Review of Impact Testing	
2.2	Instrumented Indentation Technique	32
	
	2.2.1. Introduction to Instrumented Indentation Technique	
	2.2.2. Application of Instrumented Indentation Technique	
	2.2.3. Indentation Crack Formation by a Sharp Indenter	
	2.2.4. Dynamic Indentation Technique	

2.1 Fracture Mechanics in Impact Fracture

2.1.1. The Energy Criterion

Extension of crack appears when sufficient energy is applied to overcome the material resistance. For crack growth, the applied energy includes the surface energy and other types of energy during crack formation. Energy based criterion is firstly defined by Griffith [1], and Irwin [2] developed the criterion with the energy release rate \mathcal{G} which has meaning of potential energy change rate with formation of crack area. The developed criterion is defined for linear elastic material. At the point of critical energy release rate $\mathcal{G} = \mathcal{G}_c$, fracture occurs. The point of critical energy release rate is considered as fracture toughness. The energy release rate of an infinite plate subject to a remote tensile stress is given by

$$\mathcal{G} = \frac{\pi\sigma^2 a}{E} \quad (2-1)$$

and the crack length is $2a$, E is Young's modulus, and σ is applied stress. For critical conditions of stress and crack length at fracture, \mathcal{G}_c is defined as:

$$\mathcal{G}_c = \frac{\pi\sigma_f^2 a_c}{E} \quad (2-2)$$

The energy release rate \mathcal{G} is regarded as the driving force for fracture and \mathcal{G}_c is the material's resistance to fracture.

2.1.2. Qualitative Toughness Tests

Due to the importance of material toughness in preventing brittle fracture, Charpy developed a pendulum test to measure the absorbed energy of failure in notched metallic specimens. The absorbed energy was regarded as indicative of the resistance to brittle fracture. This method revealed that fracture was more likely in steels with Charpy energy less than 20 J. Pellini developed a drop weight test to qualitatively measure crack arrest toughness from the formulation of linear elastic fracture mechanics developed by Irwin and his colleagues.

The Charpy test and the Pellini drop weight test are widely applied in structural components fracture analysis. ASTM standardized both tests including the Izod, drop weight tear and dynamic tear tests [3-6]. Although these tests lack the mathematical rigor and predictive capabilities of fracture mechanics methods, their results give a qualitative indication of material toughness. And the inexpensive, easy performance of these tests makes them more suitable for material screening and quality control than fracture

mechanics tests.

2.1.3. Historical Review of Impact Testing

As shown in the previous section, impact testing has less meaning than fracture mechanics testing since its result is merely qualitative. Researchers have also found that impact test results can be strongly affected by such test conditions as specimen size, notch geometry, test speed, and so on, and also by the energy lost to machine compliance and friction. Thus impact testing standardization has been updated with ASTM E23. Many researchers worked on the modification of standard test methods for notched-bar impact testing of metallic materials (E23) to improve test result stability.

After a historical review of impact testing, advances in impact testing and the evolution of testing standards are described. The review of impact testing below is written using the work of Siewert et al. [7].

2.1.3.1. Historical Review of Impact Testing

In the early 1800s, researchers were concerned that structural failures in the field show different behavior from that expected from tensile strength data (static loading); they realized that tensile testing is limited in predicting performance under dynamic loads.

Rodman designed a drop-weight machine to characterize gun steels on impact loading that was widely used for qualification of steel products such as railroad steels for several years [8]. The machines of the early 1800s tested the final product, and thus additional verification work is necessary for a different product design. In addition, the instrumentation of the device was poor so that gaining reliable the data took many efforts. While the test worked well for brittle materials, in which cracks could easily be induced, application to most metallic materials (ductile) led to many errors because specimens often bent without forming cracks.

LeChatalier [9] introduced notched specimens to impact test that could induce crack more easily. Some steels that showed only deformation behavior as smooth rectangular bar would exhibit fragile behavior as notched specimens. The most remarkable improvement in the early 1800s was the addition of a notch to specimen geometry, which lent more physical meaning to impact fracture. Still, the impact test procedure need improvement to provide a continuous quantitative measure of the fracture resistance of materials. Also, substantial work was needed to produce consistent data.

In 1902, the ASTM “Committee on the Present State of Knowledge Concerning Impact Tests” published in its Proceedings a bibliography on impact tests and impact testing machines [10]. This bibliography listed more than 100 contemporary papers on impact testing published in the U.S., France, and Germany. Among them, Russell [11] insisted that previous impact test devices of drop-weight design have little ability to determine data on whether a specimen is broken or not. He designed the pendulum impact machine based on the swinging of a pendulum that could measure the actual energy absorbed during the breaking of the test bar. The swinging pendulum design is commonly used in today’s impact test machines. However, Russell’s machine was developed before test specimens were standardized, and was large and massive (to guarantee it could break many materials). This impact machine is regarded as a benchmark for future research because it made it possible to quantify energy during specimen fracture for a wide range of materials and conditions.

Due to the massive effect of procedural variations on the energy value, many researchers then focused on standardizing the impact testing procedure. Charpy acknowledged the benefits of Russell's pendulum design [12] and proposed a method similar to present designs, the Charpy method. However, the concept of the pendulum machine had not yet achieved dominance: impact machines were offered in three major types: Drop Weight (Fremont,

Hatt-Turner, and Olsen), Pendulum Impact (Amsler, Charpy, Dow, Izod, Olsen, and Russell), and Flywheel (Guillery).

In the early 1900s the configuration and specimen geometry approached the defined standards of present impact testing. Specimen size was the most interesting consideration, with opinions backing one of two standard specimen sizes. Larger specimens, having the advantage of large cross section, which could reduce scatter in the data, were popular initially. However, smaller specimen sizes ultimately became popular because they were more compact and easier to sample and the testing device cost less to manufacture. The most commonly used specimen dimensions were a cross section of 10 by 10 mm, a length of about 53 mm (for a distance of 40 mm between the points of support), a notch 2 to 5 mm deep, and a notch tip radius near 1 mm. These specimen dimensions are very similar to present standards.

2.1.3.2. ASTM Method E23

The ASTM designation E23-33T “Tentative Methods of Impact Testing of Metallic Materials” was published in 1933, containing a description of previous efforts in impact testing research. (The ASTM specification of “tentative” (no longer used by ASTM) indicated that it was subject to annual

review and was a work in progress. ASTM E 23-33T specified the pendulum-type machine and recognized two methods; the Charpy test and the Izod test.

As understanding of The details that influence Charpy test results has increased, ASTM E23 has been repeatedly revised [13-17]. Overall, the verification limits in ASTM E23 have greatly improved with the increased performance of impact test devices and as data from using ASTM E23 machines could be compared with stability.

Other global organizations also developed standards for impact testing, such as the International Organization for Standardization, ISO, and the Japanese standard ,JIS:

- *ISO Standard R 442:1965 Metallic Materials - Impact Testing - Verification of Pendulum Impact Machines*
- *JIS Z2242, Method for Impact Test for Metallic Materials.*

2.1.3.3. Applications

- Nuclear

Surveillance programs utilize Charpy and tensile specimens to trace neutron-induced embrittlement because it is non-pragmatic to measure the fracture toughness of large specimens over the life of a nuclear power plant.

When it is remembered that most utilities assess the outage cost and loss of

revenue for a nuclear plant in the range of \$300,000 to \$500,000 per day, the Charpy impact test plays an economically significant role in the nuclear industry. Extending the life of a plant one more year by Charpy impact test data could save a plant owner as much as \$150,000,000. Furthermore, cost avoidance from vessel-related fracture is anticipated to be in the billion-dollar range. Up to now, the NRC has shut down one U.S. plant based on Charpy impact test data. It is crucial to note that the pressure vessel of this plant was made from a special steel and is not representative of the U.S. reactor fleet.

- Steel

The Charpy V-notch (CVN) test specimen and related test process is a useful cost-saving tool for the steel industry. This test has many advantages: specimen preparation is easy, tests can be done for various specimen orientations, and equipment cost is relatively low. In the structural steel industry, the CVN test is used for many applications: (1) as a quality control tool to compare different heat-treated specimens of the same type of steel, (2) to verify accordance with standard impact requirements, and (3) to anticipate service performance of components. Also, fracture toughness data can be predicted from CVN test data for a class of steels. Hence the results of fracture mechanics analysis can be compared to the toughness of material.

CVN data can be used for many purposes, particularly during design and construction of a bridge or an offshore oil platform. The supplier should prove to the buyer that a steel plate meets specific design criteria before full-scale production of the steel order begins. The process begins by grading the steels and then testing a part of the plate to verify if it meets all requirements. In addition, steel mill equipment sets limits on plate size: thus, each steel plate must be welded together in the field to produce lengths that can reach deep inside oceans. Small parts of the plate are welded and the crack tip opening displacement (CTOD) test, a kind of fracture mechanics test, is carried out in the heat-affected zone (HAZ) and in the region along fusion line (the boundary between the weld metal and base metal). After that, a steel supplier may correlate the CTOD test data with the CVN 50% ductile-brittle transition temperature (DBTT). With an agreement between the supplier and customer, the correlation permits the steel supplier to use the Charpy test instead of the more expensive and time-consuming CTOD test.

2.2 The Instrumented Indentation Technique

2.2.1. Introduction to the Instrumented Indentation Technique

Basic idea of instrumented indentation technique is inferred from the

conventional hardness testings of Vickers and Brinell which measure hardness from the size of the imprint and applied load. Conventional hardness testing is regarded as resistance to penetration which could be the measured property after the indenting process. However, the instrumented indentation technique records material behavior with real time measurement of load and depth during penetration process of indenter that indirectly calculates the contact area of penetration with load-depth curve to determine material hardness [18-21].

Elastic modulus of material also determined from the used equation of contact area [18-21]. Instrumented indentation technique has major advantages of measuring the material yield strength, tensile strength, strain hardening exponent[22], fracture toughness[33, 34-36] and residual stress[23-27] with the similar circumstances which are analyzed from the recorded load-depth curve. The previous researches on instrumented indentation technique are in progress due to 1) its simplicity, 2) applicability to micro/nano scale features, 3) effectiveness of cost saving (requires small amount of specimen), and 4) applicability on in-field devices because of nondestructiveness.

Though direct comparison with conventional mechanical tests still contains limitations, usage of instrumented indentation technique is widely increased due to its advantages.

However, still specimen preparation is somewhat time-consuming that flat plane should be obtained with polishing process to get uniform indentation results.

Instrumented indentation testing is defined with the applied load range; macro, micro, nano indentation. From the stated advantages of indentation, macroindentation is widely used for the in-field component and micro/nano indentation is regarded as powerful tools for evaluating required mechanical properties in small scale for thin films, MEMS, bio devices.

As instrumented indentation is used widely with the many advantages, standardization of testing method has been discussed all over the world for several decades.

ISO 14577-1 [38] is the most fundamental standard which specifies the method for hardness and material parameters of instrumented indentation technique, and the verification and calibrations of testing machine. The micro/nano range testing method suitable for thin coatings described in the part of ISO 14577-4[39] is also still under discussion.

Recently, a new ISO technical report, TR 29381:2008[40], describes tensile properties of metallic materials through representative stress and strain method with the result of instrumented indentation testing. Also the report includes a procedure for evaluating residual stress using instrumented indentation testing in an appendix.

2.2.2. Application of Instrumented Indentation Technique

2.2.2.1. Hardness and Elastic Modulus

Schematic of typical load-depth curve for sharp indentation, such as Vickers and Berkovich indenter, is shown in Figure 2.1(a). Deformation along loading is assumed to be both elastic and plastic for modeling purposes as the permanent hardness impression forms. And elastic displacement is recovered during unloading process.

The method is restricted for the materials which do not show plasticity reverse during unloading. It is calculated from the finite element simulations that the appearance of reverse plastic deformation is usually negligible [41]. From the $P-h$ curves, the maximum load (P_{max}), the maximum displacement (h_{max}), and the elastic unloading stiffness ($S = dP/dh$, defined as the slope of the upper portion of the unloading curve during the initial stages of unloading ;also called the contact stiffness) is derived to measure hardness and modulus. The measurement of each parameter is important for obtaining accurate hardness and modulus. And also determination of final depth (h_f) is important after the full unloading. Determination method of

hardness and elastic modulus is extent from the method of Doerner and Nix [18]. Doerner and Nix used the flat-punch approximation which takes into account the fact that unloading curves are curved and cannot be treated by the flat-punch approximation. For flat-punch, the contact area is constant so as the resulting unloading curve is linear. However, experimental result showed that unloading curves are distinctly curved and well approximated by the power-law relation

$$P = \alpha (h - h_f)^m, \quad (2-3)$$

where α and m are power-law fitting constants [19].

Fig. 2.2 is schematic feature of measuring hardness and elastic modulus based on unloading processes; the behavior of the Berkovich indenter is assumed to be modeled by a conical indenter with a half-included angle θ that gives the same depth-to-area relationship, $\theta = 70.3^\circ$. The basic assumption is that the sink of contact surface is described by the models of a flat elastic half-space by rigid punches of simple geometry [42-46]. The assumption makes limitation of applying on some materials showing pile-up at the contact surface. With assumption of negligible pile-up, the elastic models define amount of sink-in, h_d , to be

$$h_d = \omega \frac{P_{\max}}{S}, \quad (2-4)$$

where ω is a constant that depends on indenter geometry.

The values are: $\omega = 0.72$ for a conical punch, $\omega = 0.75$ for a parabolic of revolution (which approximates to a sphere at small depths), and $\omega = 1.00$ for a flat punch [42].

Approximation of the vertical displacement of contact surface is defined with using Eq. (2-4) and it is determined from the geometry of Fig. 2.2.

The defined depth, $h_c = h_{\max} - h_d$, is

$$h_c = h_{\max} - \varepsilon \frac{P_{\max}}{S}. \quad (2-5)$$

The projected (or cross-sectional) area of indenter is described by the area function $F(d)$. The contact area A at a distance d from its tip is

$$A = F(h_c). \quad (2-6)$$

Then, the hardness is estimated after the contact area determination,

$$H = \frac{P_{\max}}{A}. \quad (2-7)$$

As the basic definition of hardness is based on the contact area under applied load, the traditional hardness measured from the area of the residual impression with the existence of significant elastic recovery during unloading. This is effective for the materials with extremely small values of

E/H [25].

Elastic modulus is measured from the relationship between the contact area and unloading stiffness, where E_r is the reduced modulus as show in Eq. (2-28).

$$S = \beta \frac{2}{\sqrt{\pi}} E_r \sqrt{A}, \quad (2-8)$$

The effective elastic modulus is applied due to the elastic displacement occurs in both the specimen and the indenter. Young's modulus and Poisson's ratio of specimen is E and ν . Young's modulus and Poisson's ratio of indenter are E_i and ν_i . Eq. (2-8) is a general relationship that applies to any axisymmetric indenter [47,48]. Even though the equation derived for elastic contact [49], it is also shows good applicability to elastic-plastic contact [50], and to be unaffected from pure axisymmetric geometry [51]. It is not affected by pile-up and sink-in.

2.2.2.2. Indentation Tensile Properties

Indentation tensile properties are evaluated with the algorithm consisted of four steps: step 0 determination of real contact area; step 1 definition of representative stress and strain; step 2 constitutive equation; and step 3 evaluation of tensile properties.

Figure 2.1(b) is a typical indentation load-depth curve obtained from the spherical indentations on steel. Unlike curves from sharp indentations using pyramidal indenters, loading curves are quite linear due to the counterbalance of spherical geometry and work-hardening in the tested steel. Several depths are defined from this curve. The maximum indentation depth h_{max} is the total displacement of the material and the indenter at maximum load L_{max} , including elastic and plastic deformation. In unloading, elastic deformation is the indentation stiffness of the specimen and the indenter S . Thus, the final depth h_f is the plastic deformation of the material.

A contact depth h_c^* at maximum indentation load can be evaluated by analyzing the unloading curve using the concepts of indenter geometry and elastic deflection [19]:

$$h_c^* = h_{max} - \omega(h_{max} - h_i) \quad (2-9)$$

where h_i is the intercept indentation depth and the indenter shape parameter is 0.75 for a spherical indenter. The material pile-up around the indentation enlarges the contact radius (from the analysis of elastic deflection) by an extent determined by the work-hardening exponent n and the ratio of maximum indentation depth and indenter radius h_{max}/R [21]:

$$h_{pile}^* = h_c^* \cdot f(n, h_{max} / R) \quad (2-10)$$

where h_{pile}^* is the plastic pile-up depth.

The mean pressure p_m obtained by dividing the maximum load L_{max} by the contact area a_c^2 is well known to be about three times the representative stress σ_R for fully plastic deformation of steels [21]. In other words, the representative stress can be expressed as:

$$\sigma_R = \left(\frac{I}{\psi} \right) P_m = \left(\frac{I}{\psi} \right) \left(\frac{L_{max}}{\pi a_c^2} \right) \quad (2-11)$$

where ψ is a plastic constraint factor, here taken as 3, and a_c is the contact area. On the basis of the deformation shape and strain distribution under a spherical indenter, Kwon [27] proposed a new definition using the tangent function and a strain-proportional constant α :

$$\varepsilon_R = \left(\frac{\alpha}{\sqrt{I - (a_c / R)^2}} \right) \left(\frac{a_c}{R} \right) = \alpha \tan \gamma \quad (2-12)$$

where α was determined as 0.14 by finite element analysis for various materials [52], R is the indenter radius and γ is the half-angle between the

indenter and the material. The true stress and strain points obtained from the indentation test are then fitted to a constitutive equation by a simple power-law-type Hollomon equation:

$$\sigma = K \cdot \varepsilon^n \quad (2-13)$$

where n is the work-hardening exponent and the gradient of the curve, K is the strength coefficient, and σ and ε are respectively the representative stress and strain values. This approach assumes that the flow curve of many metals in the uniform plastic deformation region can be expressed by Eq. (2-13). With most materials there is a gradual transition from elastic to plastic behavior, and the point at which plastic deformation begins is hard to define with precision. Although there are various criteria for the initiation of yielding, the yield strength obtained by an offset method is commonly used for design and specification purposes because doing so avoids the practical difficulties of measuring the elastic limit or proportional limit [53]. Thus, the yield strain can be determined as the intersection point of an elastic line whose slope is the elastic modulus 0.2% offset from the origin and a plastic curve of the constitutive equation. The uniform tensile strain should be same as the work-hardening exponent, by the theory of instability in tension [53],

and from this the indentation tensile strength can be determined. The indentation yield strengths and the indentation tensile strengths lie within 10% and 5% error respectively of those from uniaxial tensile tests [54].

2.2.2.3. Residual Stress

Indentation hardness as analyzed from the indentation $P-h$ curve changes with the material residual stress: indentation $P-h$ curves are shifted with the direction and magnitude of the residual stress in the tested material. However, variations in the apparent indentation hardness with change in residual stress have been identified as an artifact of erroneous optical measurements of the indentation imprint [23,24]: in a study of the influence of in-plane stress on indentation plasticity that investigated both the shape of the indentation curve and the contact impressions, the contact hardness was found to be invariant regardless of the elastically applied stress (residual stress) [23,24]. FEA results showed the important role of sink-in or pile-up deformations around the contact in the stressed state in producing the stress-insensitive contact hardness [25]. Therefore, the change in contact morphologies with residual stress is modeled for constant maximum indentation depth assuming the independence of intrinsic hardness and residual stress [26].

The change in indentation deformation caused by the residual stress was

identified in the indentation loading curve in Fig. 2.3. The applied load in the tensile-stressed state is lower than in the stress-free state for the same maximum indentation depth [23, 24, and 26]. In other words, the maximum indentation depth desired is reached at a smaller indentation load in a tensile-stressed state because a residual-stress-induced normal load acts as an additive load to the applied load. Therefore, the residual stress can be evaluated by analyzing the residual-stress-induced normal load.

The detailed changes in contact morphology can be seen in the schematic diagram in Fig. 2.4. The residual stress is relaxed from a tensile-stressed state to stress-free state while maintaining the constant maximum depth, h_{max} , as the stress relaxation pushes the indenter out from the surface. The pushing force appears as an increase in the applied load ($L_T \rightarrow L_0$) and the contact depth ($h_c^T \rightarrow h_c$), because the maximum depth is held constant. The indentation load and maximum depth for the tensile-stressed state (L_T, h_{max}) are equivalent to those in the relaxed state (L_0, h_{max}). Thus, the relationship between the two states can be expressed as

$$L_0 = L_T + L_{res} . \quad (2-14)$$

In the compressive stress state, the applied load and contact depth decrease by stress relaxation under the maximum-depth-controlled path. Furthermore,

this decreasing portion of the applied load was the residual-stress-induced normal load, L_{res} . Therefore, the residual stress in a welded joint can be evaluated by dividing L_{res} by the contact area, A_c , regardless of the stress state [27]:

$$\sigma_{res} = \alpha \frac{L_{res}}{A_c}, \quad (2-15)$$

where α is a constant related to the stress directionality of the biaxial residual stress. The biaxial stress state, in which $\sigma_y = k\sigma_x$, can be divided into a mean stress term and a plastic-deformation-sensitive shear deviator term [22]:

$$\begin{array}{ccc} \underline{Biaxial\ stress} & \underline{Mean\ stress} & \underline{Deviator\ stress} \\ \left(\begin{array}{ccc} \sigma_{res}^x & 0 & 0 \\ 0 & \sigma_{res}^y & 0 \\ 0 & 0 & 0 \end{array} \right) & = \left(\begin{array}{ccc} \frac{1+k}{3}\sigma_{res}^x & 0 & 0 \\ 0 & \frac{1+k}{3}\sigma_{res}^x & 0 \\ 0 & 0 & \frac{1+k}{3}\sigma_{res}^x \end{array} \right) & + \left(\begin{array}{ccc} \frac{2-k}{3}\sigma_{res}^x & 0 & 0 \\ 0 & \frac{2-k}{3}\sigma_{res}^x & 0 \\ 0 & 0 & -\frac{1+k}{3}\sigma_{res}^x \end{array} \right) \end{array} \quad (2-16)$$

The stress component parallel to the indentation axis in the deviator stress term directly affects the indenting plastic deformation. A residual-stress-

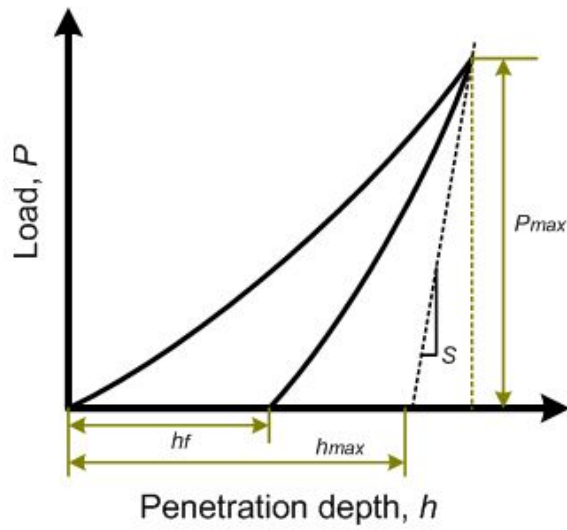
induced normal load L_{res} can be defined from the selected deviator stress component as:

$$L_{res} = \frac{1+k}{3} \sigma_{res} A_c. \quad (2-17)$$

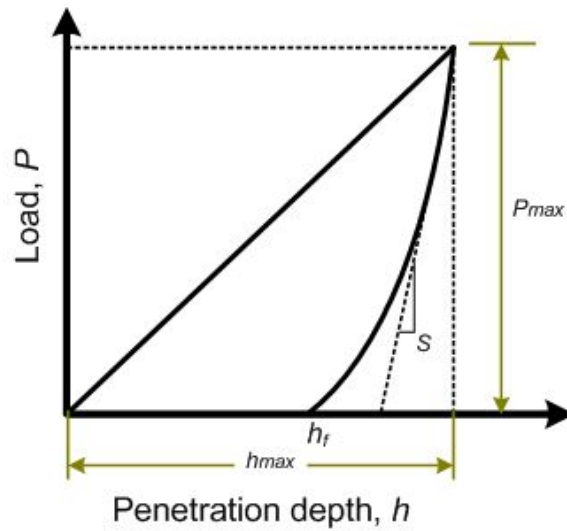
Therefore, α in Eq. (2-50) can be taken as approximately 1.5 in the equibiaxial stress state. In the instrumented indentation test, the contact area is determined by unloading curve analysis. By differentiation of the power-law-fitted unloading curve at maximum indentation depth, the contact depth and contact area can be calculated from the contact depth based on the geometry of the Vickers indenter as [19]:

$$A_c = 24.5h_c^2. \quad (2-18)$$

Thus, residual stress is calculated from the analyzed contact area in Eq. (2-52) and the measured load change L_{res} by the effect of residual stress in Eq. (2-49).



(a) Sharp indentation



(b) Spherical indentation

Figure 2.1. Schematic diagram of typical load-depth curve during instrumented indentation.

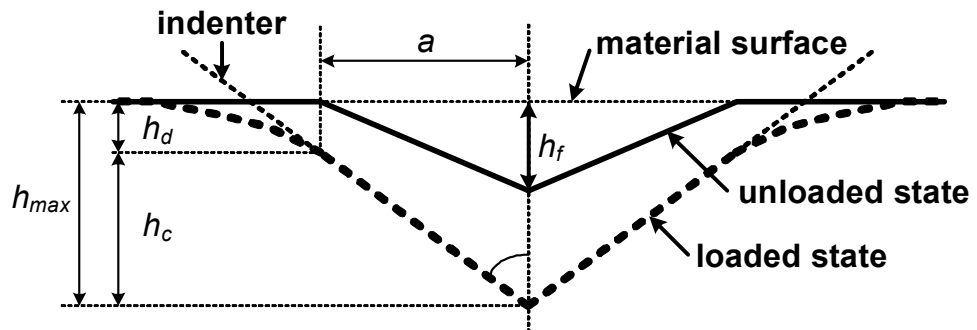


Figure 2.2. Cross section of contact morphology in the loaded state and residual indent by a sharp indenter after unloading.

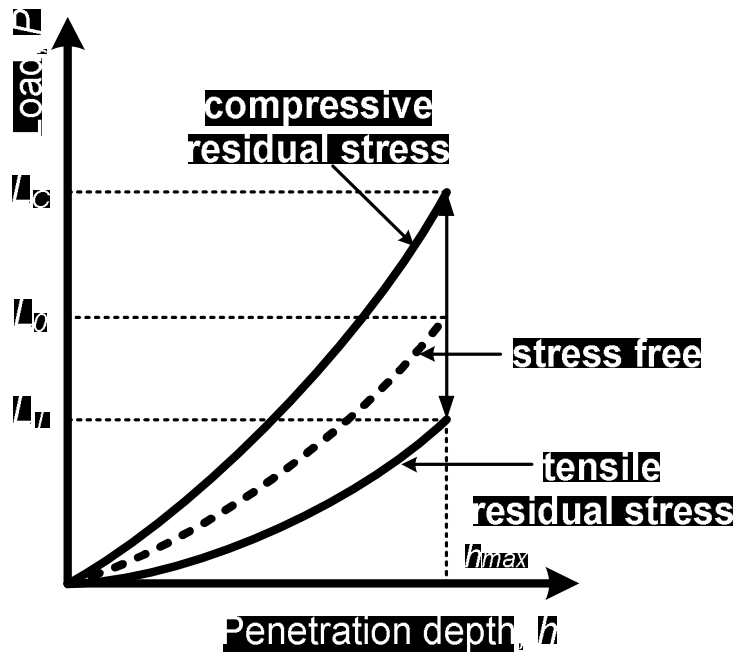


Figure 2.3. Variation in indentation loading curves with changes in stress state.

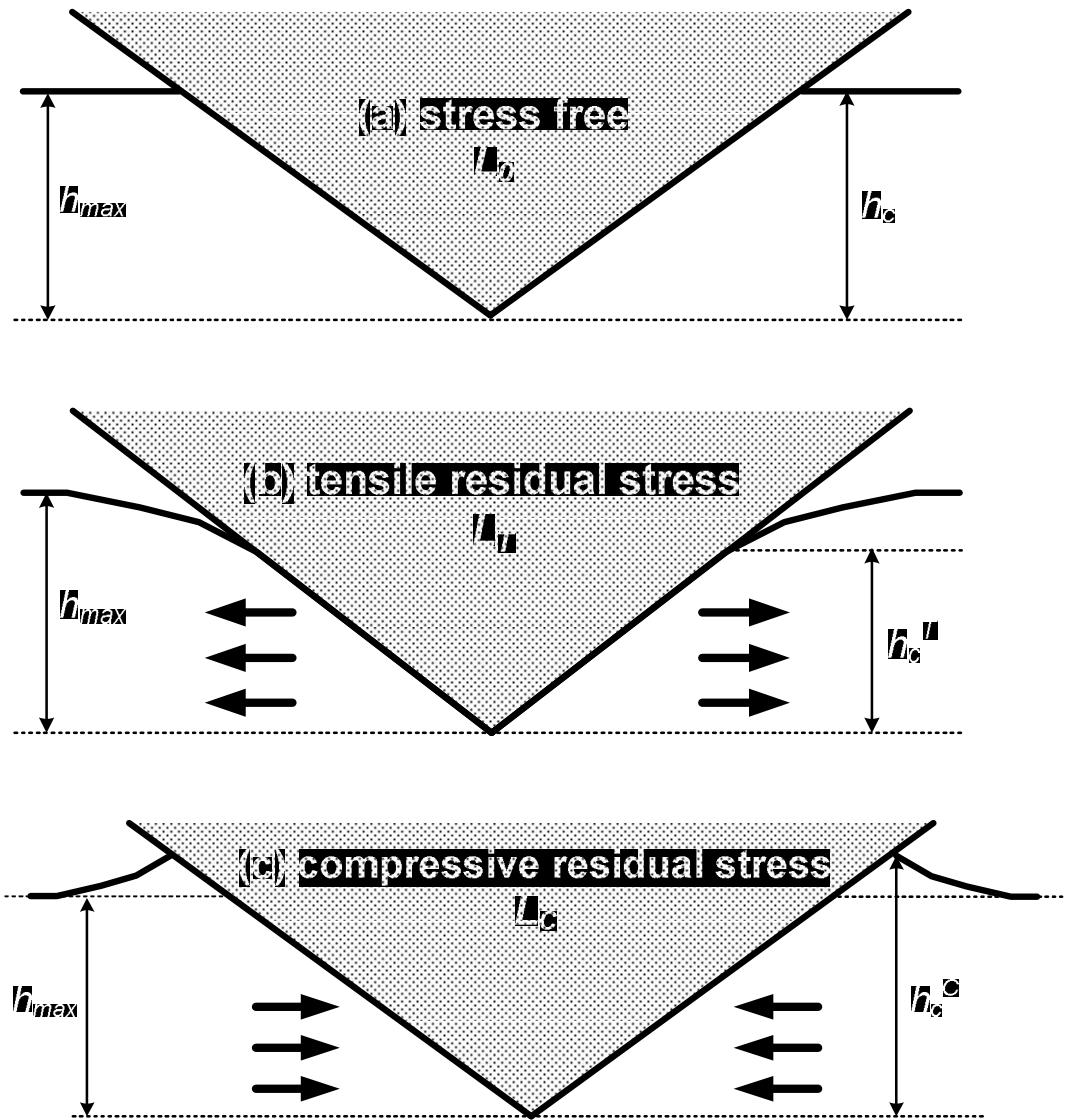


Figure 2.4. Theoretical surface morphologies around the contact for (a) stress-free, (b) tensile stress, and (c) compressive stress states.

2.2.2.4. Indentation Fracture Toughness

Instrumented indentation can be used to evaluate the fracture toughness of materials and interfaces in a manner similar to that conventionally used in larger-scale testing. During loading, tensile stresses are induced in the specimen material as the radius of the plastic zone increases. Upon unloading, additional stresses arise as the elastically strained material outside the plastic zone attempts to resume its original shape but is prevented from doing so by the permanent deformation associated with the plastic zone. There exists a large body of literature on the subject of indentation cracking with Vickers and other sharp indenters.

In general, there are various types of crack, as illustrated in Fig. 2.5 [37]. Radial cracks are vertical half-penny-type cracks occurring on the surface of the specimen outside the plastic zone and at the corners of the residual impression at the indentation site. These radial cracks are formed by a hoop stress and extend downward into the specimen but are usually quite shallow.

Lateral cracks are horizontal cracks that occur beneath the surface and are symmetric with the load axis. They are produced by a tensile stress and often extend up to the specimen surface, resulting in a surface ring that may lead to chipping of the surface. Median cracks are vertical circular penny cracks that form beneath the surface along the axis of symmetry and are aligned with the corners of the residual impression. Depending on the loading conditions,

median cracks may extend upward and join with surface radial cracks, thus forming two half-penny cracks that intersect the surface, as shown in Fig. 2.5(d). They arise due to the action of an outward stress. The exact sequence of initiation of these three crack types is sensitive to experimental conditions. However, it is generally observed that in soda-lime glass loaded with a Vickers indenter, median cracks initiate first. When the load is removed, the elastically strained material surrounding the median cracks cannot resume its former shape owing to the presence of the permanently deformed plastic material, leading to a residual impression in the specimen surface.

Residual tensile stresses in the normal direction then produce a horizontal lateral crack that may or may not curve upward and intersect the specimen surface. Upon reloading, the lateral cracks close and the median cracks reopen. For low values of indenter load, radial cracks also form during unloading (in other materials, radial cracks may form during loading). For large loads, upon unloading, the median cracks extend outward and upward and may join with the radial cracks to form a system of half-penny cracks that are then called median/radial cracks. In glass, the cracks observed at the corners of the residual impression on the specimen surface are usually fully formed median/radial cracks.

It is the radial and lateral cracks that are of particular importance, since their proximity to the surface has a significant influence on fracture strength.

Fracture mechanics treatments of these crack types seek to provide a measure of fracture toughness based on the length of the radial surface cracks. Attention is usually paid to the length of the radial cracks as measured from the corner of the indentation and then radials outward along the specimen surface, as shown in Fig. 2.6.

Palmqvist [28] stated that the crack length varies as a linear function of the indentation load. Lawn, Evans, and Marshall [32] formulated a different relationship: they treated the fully formed median/radial crack and found that the ratio $P/c^{3/2}$ (where c is measured from the center of contact to the end of the corner radial crack) is a constant whose value depends on the material.

Fracture toughness is found from:

$$K_c = \alpha \left(\frac{E}{H} \right)^{1/2} \left(\frac{P_{max}}{c^{3/2}} \right) \quad (2-19)$$

where α is an empirical calibration constant dependent on the geometry of the indenter. The value of 0.016 was found to give good correlation between the toughness values measured from the crack length and those obtained using more conventional methods [55]. An attractive feature of using this method in indentation is that both H and E can be determined directly from analyses of indentation force-depth data. Thus, provided one can measure crack lengths, implementing the method is relatively straightforward.

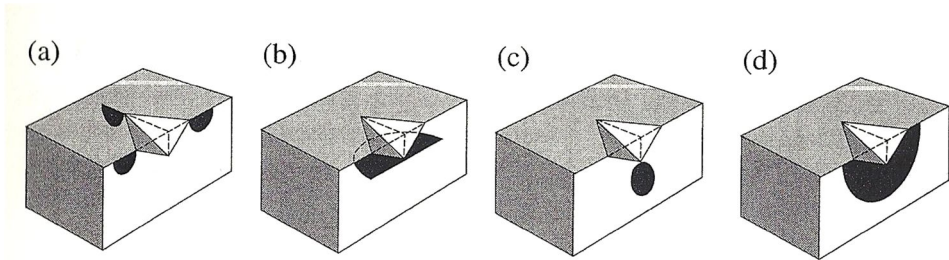


Figure 2.5. Crack system for Vickers indenter: (a) radial cracks, (b) lateral cracks, (c) median cracks, and (d) half-penny cracks.

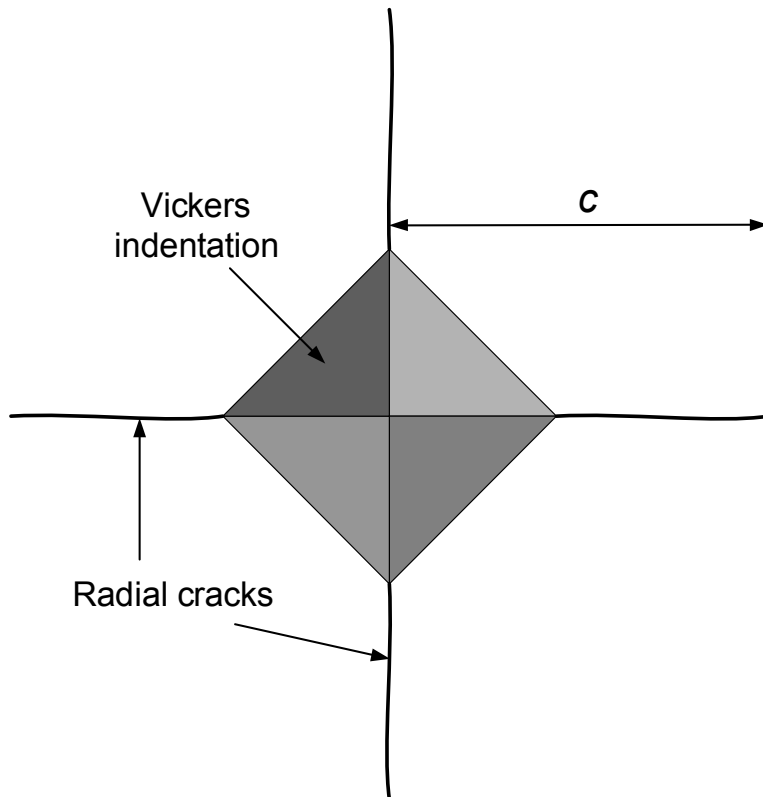


Figure 2.6. Schematic feature of radial cracking by Vickers indentation.

2.2.3. Indentation Crack Formation with Sharp Indenter

Indentation crack formation is interpreted using a research review by Johanns [60]. Many researchers have looked at indentation crack formation to estimate fracture characteristics. Indentation cracking is generally studied with brittle solids because it is hard to induce or verify well-made cracks in ductile materials. Researchers studying indentation cracking in brittle solids found that indentation cracking occurs in both loading and unloading of the indenter with different crack shapes due to compressive and tensile stress during the indentation process [29, 61, and 63]. A median/radial crack system is often found during a sharp indentation loading process such as Vickers, Berkovich, and cube-corner pyramidal indentations. Johanns [60] approached indentation crack formation in loading with numerical analysis. The cohesive zone model, a traction-separation-based constitutive behavior, is used to model crack growth in numerical simulations. Crack formation in a sharp indentation process with elastic-plastic materials has four steps: 1) geometrically self-similar contact deformation where the contact size is proportional to with the applied load; 2) stable flaw nucleation by plastic deformation; 3) the short crack regime where the process zone dominates crack behavior; and 4) steady-state crack growth.

The most significant problem in the crack formation process is flaw nucleation during plastic deformation. Two elements must be considered in indentation cracking with a geometrically self-similar sharp indenter: 1) the

state of stress and strain is fixed from the onset of indentation and 2) the magnitudes of the stresses and strains are limited by the yield strength of the material. Previous researchers have found that the maximum tensile stress occurs at the elastic-plastic boundary of the indentation axis and that its magnitude is below the yield strength of the material, usually on the order of $YS/2$ or less [62]. Thus, the flaw cannot be nucleated merely by an increment of the indentation load. Indentation crack formation analysis must determine the basic appearance of the flaw. There are two ways of explaining crack formation: it is 1) a pre-existing flaw distribution or 2) a material-specific physical process from the indentation deformation that initiates nucleation. Hagan and Swain [65] explained that the intersection of slip bands under the indentation generates a flaw with the stress concentration due to dislocation pile-up.

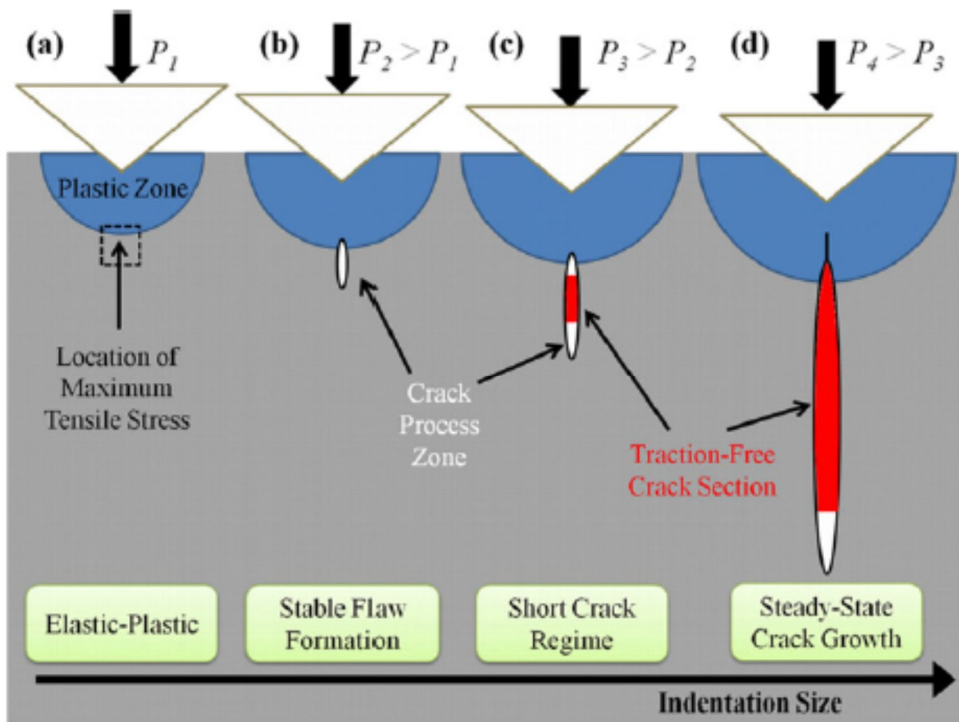


Figure 2.7. Crack formation during sharp indentation.

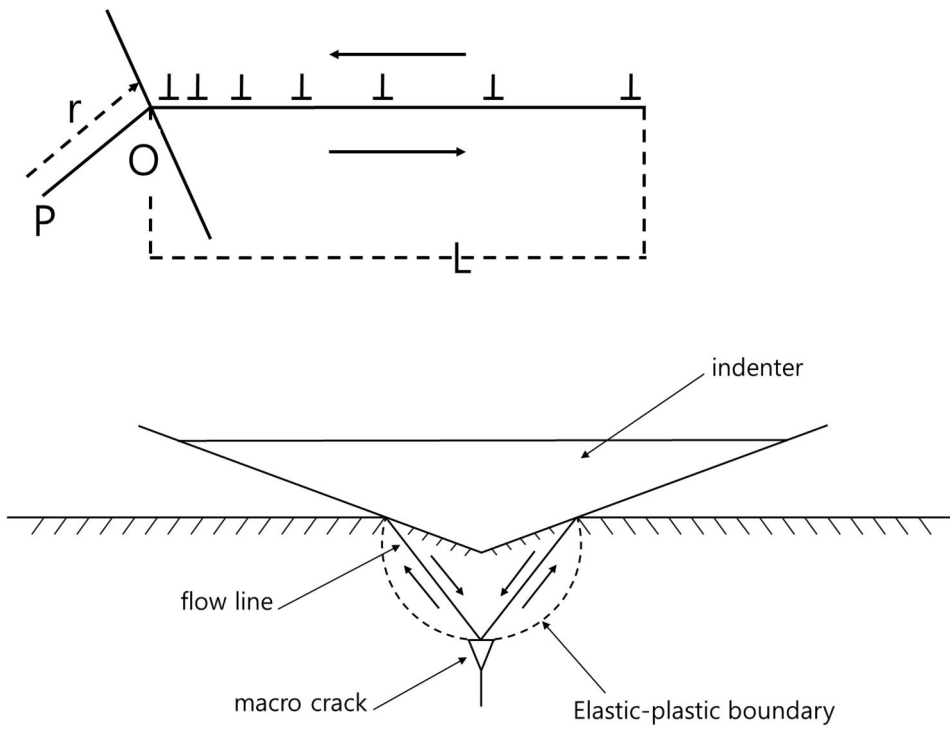


Figure 2.8. Nucleation of indentation-induced flaw from stress concentration due to dislocation pile-up at slip band intersect [65].

2.2.4. Dynamic Indentation Technique

1) Dynamic hardness

Hardness testing is used in various engineering fields due to its simplicity. Static indentation hardness is the method most commonly used because it is known to be related to ductility, machinability, wear resistance and impact resistance [69, 80]. While the definition of hardness varies with the application, the main concept of hardness is resistance to penetration, which can induce deformation, wear, scratching, cutting, etc. [73, 82, and 83]. Although static hardness provides valuable results for a material deformation behavior, it may be inaccurate for dynamic and high-strain-rate deformation. Dynamic deformation is defined by strain rates in the range $10^2\sim 10^6/s$ [99]. With increased deformation rate, yield and flow stresses are increased in metals and fracture toughness increases even in ceramics [84, 85]. Martel [79] was the first to recognize the concept of rate-dependent hardness; other researchers then developed several experimental techniques. Most work is based on rigid body dynamics, which uses the rebound method. Thus some researchers define the dynamic hardness as rebound hardness. However, the rebound method does not measure the hardness value with indentation load. The dynamic hardness is measured and the energy change explained by rebound height. Thus the measured dynamic hardness has many differences

from static hardness.

Tabor [87] expanded the concept of dynamic hardness to be IIT hardness, defined with indentation load and displacement. Though Tabor's concept of dynamic hardness is still based on energy concepts, he derived the hardness from the indentation result defined as the normalized energy value with deformed volume. The value of Tabor's hardness is found to be sensitive to the strain rate.

An improved measurement method was the Hopkinson pressure-bar device [74, 77], which can induce dynamic deformation. The strain rate can be calculated as the indentation strain rate as defined by Doerner and Nix [1]. Subhash [67] suggested the application of static hardness determination methods to a dynamic strain-rate range using the Hopkinson pressure-bar test. The dynamic Vickers hardness thus determined was found to be 1.8 times greater than the static Vickers hardness value.

2) Fracture performance evaluation with dynamic indentation

As dynamic indentation device inflict the dynamic deformation with in small scale indent, there's some attempt to apply the method to the field of nanoscale device impact fracture property estimation. Chaudhri[88] explained the dynamic hardness with indentation crack formation. Nano

scale dynamic indentation device is developed recently from the NanoMaterials; Nanotest. Beake[89-92] showed the considerable result of detecting fracture performance for some materials using developed device. Jannet[93] also showed the fracture performance determination of DLC with the same device. Two previous researches focused on detecting fracture situation of material with change in indentation result. Energy of impact fracture is estimated with the indentation curve with defined fracture.

Some applications of using Nanotest or similar device is still in progress. [94, 95]

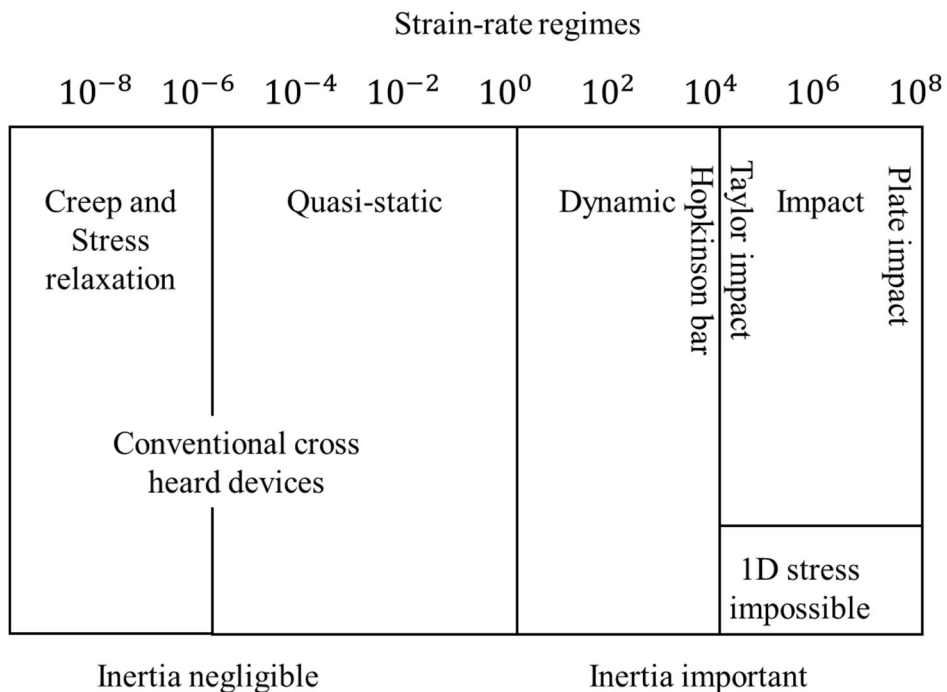


Figure 2.9. Strain rate regimes of present test devices [99].



Figure 2.10. NanoTest Vantage (Micro Materials)

Chapter 3

STRAIN-RATE-DEPENDENT INDENTATION

FRACTURE CHARACTERISTICS

Contents

3.1. Influence of Strain Rate on Indentation Fracture Characteristic	63
3.1.1. Introduction	
3.1.2. E/H ratio change in strain-rate-controlled indentation test	

3.1. Influence of Strain Rate on Indentation Fracture Characteristics

3.1.1. Introduction

Material properties, such as hardness, elastic modulus, tensile strength, fracture toughness, could be calculated from the load-displacement curve of an indentation test. Since an indentation test is a method for analyzing static deformation, dynamic material properties can be obtained from dynamically recorded load-displacement curves if the strain rate increases to the dynamic range. One dynamically obtained indentation property is the dynamic hardness, suggested by Tabor [87].

In the present study, three kinds of frit-bonding material known to have different dynamic fracture characteristics are used to verify the strain-rate dependency of indentation fracture characteristics. *In-situ* nano-indentation tests were conducted using PI85 (Hysitron) devices inside a SEM chamber. Hardness and modulus, thought to be related to fracture properties, were measured from load-controlled indentation testing performed with a cube-cornered indenter up to 5000 μN . Indentation hardness and modulus are calculated from load-displacement curve with strain rate controlled to 25/s. Dynamic fracture characteristics of the three kinds of materials are estimated by the elastic modulus to hardness ratio, which is

known to be related to fracture toughness [96,97]. Indentation-estimated dynamic fracture characteristics are compared with drop impact tendency of each specimen to verify the result.

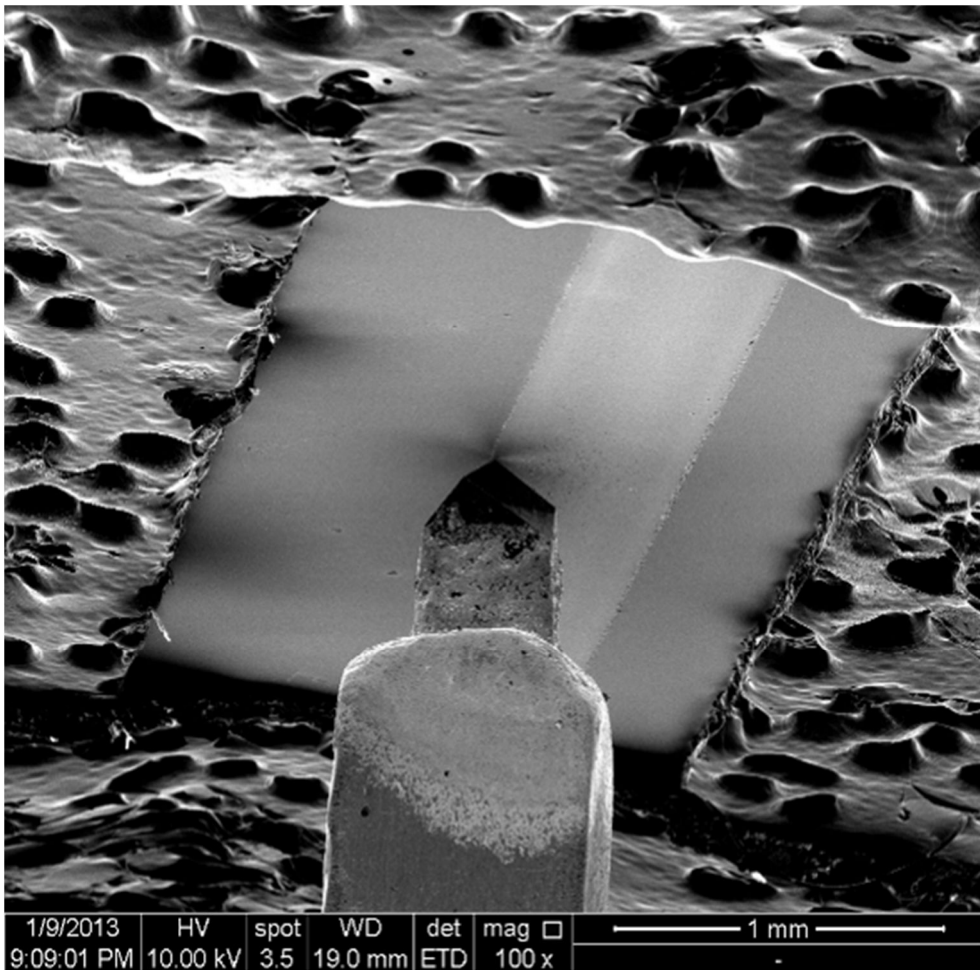


Figure 3.1. In-situ SEM nanoindentation.

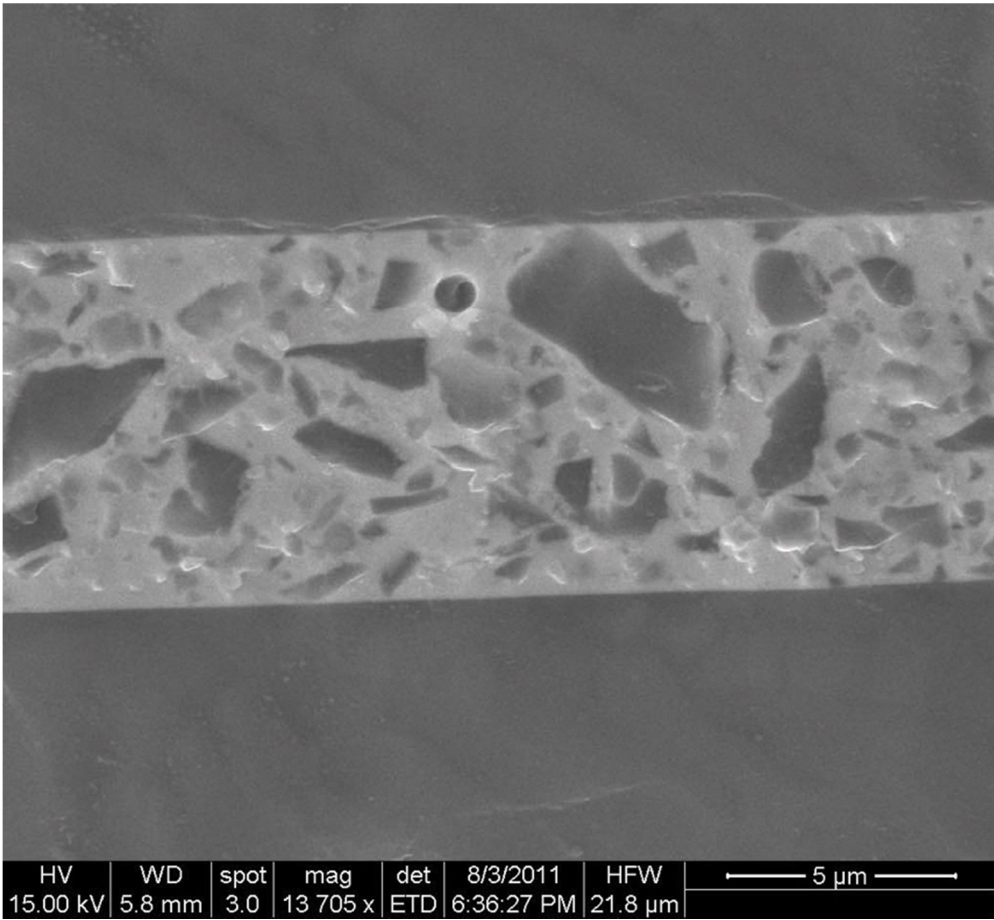


Figure 3.2. SEM image of frit-bonding specimen.

3.1.2. E/H Ratio Change in Strain-Rate-Controlled Indentation Test

Doerner and Nix suggest that various strain rate conditions can be created by controlling the indentation loading rate [1]. The indentation strain rate can be defined in terms of displacement using the load-displacement relations in indentation testing:

$$\dot{\epsilon} = c \left(\frac{1}{h} \frac{dh}{dt} \right) \quad (3-1)$$

Mechanical properties tested in dynamic strain-rate situations can be measured by indentation tests with controlled loading rate.

Three kinds of specimens of different glass-based materials were made. Three glass-based materials, V-T (vanadium-tellurium), V-P (vanadium-phosphate) and Bi (bismuth), were used as the matrix material. Strain-rate-controlled indentation tests were carried out in the strain rate range of 1/s to 25/s, which is the static to dynamic strain range.

The hardness values in Table 3.1 are plotted in Fig. 3.4. The slope with increasing strain rate in Fig. 3.4 shows the response of the materials to strain rate. The hardness value increased with increasing strain rate for each specimen. The increasing tendency (the slope in Fig. 3.4) was greatest for the Bi-based frit bonding specimen, medium for the V-P-based frit bonding specimen and low for the V-T-based frit bonding specimen. Unlike hardness

values evaluated under static conditions, the hardness values at 25/s strain rate (dynamic strain condition) showed clear differences among the materials, especially between V-P- and V-T-based frit-bonding specimens.

However, fracture behavior is more closely related to a material's fracture toughness than to its hardness value. The fracture toughness value can be calculated from Eq. (3-2), which shows the relationship between fracture toughness and indentation hardness suggested by Lawn [32]:

$$K_c = \alpha \left(\frac{E}{H} \right)^{\frac{1}{2}} \left(\frac{P_{max}}{c^2} \right) \quad (3-2)$$

where K_c is fracture toughness, H hardness, P load, and c crack length.

This equation gives the value of K_c when an indentation crack exists. But in the present study the applied load during indentation was extremely low (5000 μ N) and thus crack did not appear clearly at the sharp corner of the indented trace, as shown in Fig 3.3. It was thus impossible to get an exact fracture toughness value. However, careful observation of the indented trace revealed crack-like morphology within the indented surface, as indicated by arrow in Fig. 3.3. Thus, it is possible to use equation (8), which calculates fracture toughness even though the calculated values may not represent the exact K_c values. The extremely small loading left similar indented traces on each specimen, though the hardness values differed. This small trace can be taken as a crack, and the length of the crack in each material is similar. Then,

the trend in fracture toughness can be predicted by the E/H ratio in Eq. (3-2).

The hardness and modulus values increased with increasing strain rate as shown in Table 2. The increased values mean that the materials are sensitive to strain rate, as shown in Fig. 3.4. As mentioned above, fracture behavior can be evaluated by fracture toughness rather than hardness value. Figure 3.5 displays the evolution of E/H values with increasing strain rate. The value for each material decreased with increasing strain rate, and the slope of the decrease differed among the three materials. At the highest strain rate of 25/s, E/H values for V-T were relatively high, V-P values in the middle, and Bi values low. The value of K_c could be calculated by substituting E/H in Eq. (3-2) for each material. This variation showed similar trends to the variation in drop impact.

Thus, estimation of indentation fracture characteristics with strain rate was shown with the present study. This result suggests that direct estimation of the dynamic fracture property may be possible if the test method is supplemented more similar to dynamic fracture testing, with strain rate up to $10^3 \sim 10^6/s$.

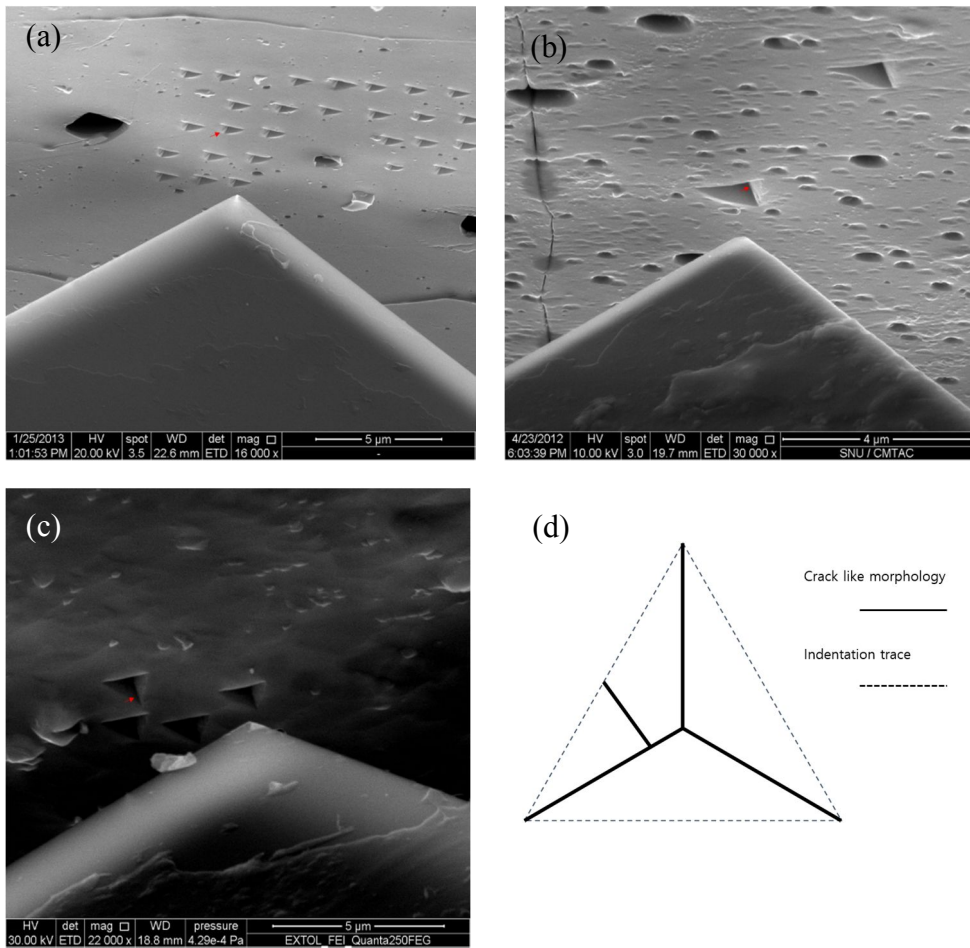


Figure 3.3. Crack-like morphology within indented surface:

(a) V-T-based frit bonding, (b) V-P-based frit bonding, (c) Bi-based frit bonding. (d) Schematic of crack-like morphology

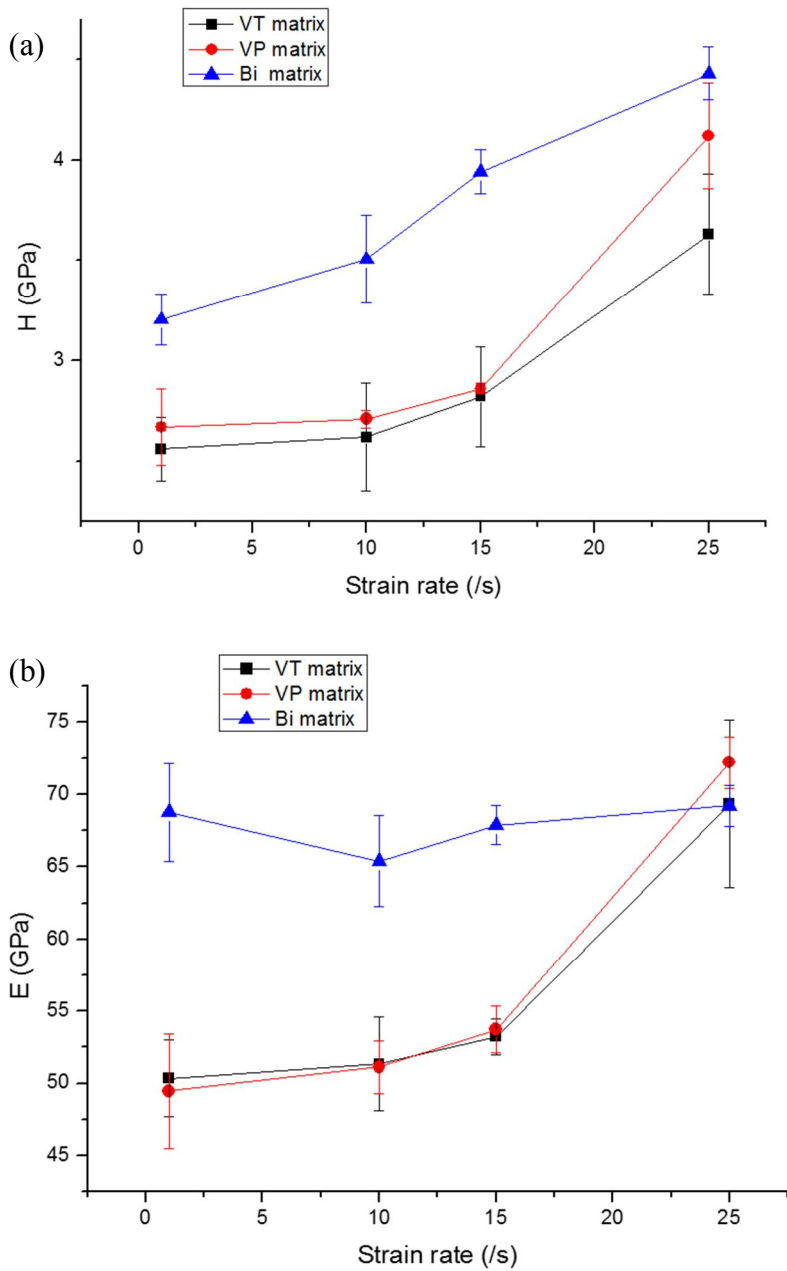


Figure 3.4. Indentation (a) hardness and (b) elastic modulus at various strain rates.

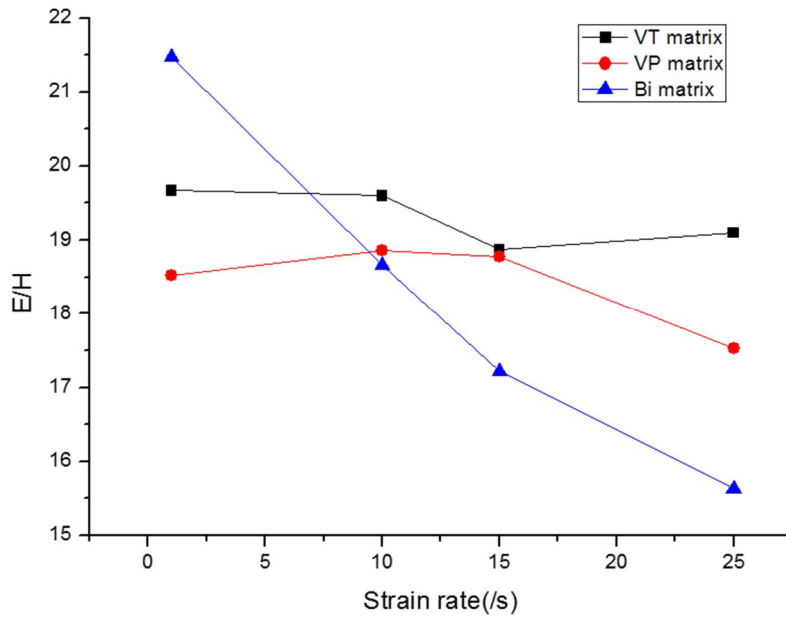


Figure 3.5. E/H ratio at various strain rates.

Strain rate (/s)	VT-based bonding specimen					VP-based bonding specimen					Bi-based bonding specimen				
	<i>E</i> (Gpa)	STDEV	<i>H</i> (Gpa)	STDEV	<i>E/H</i>	<i>E</i> (Gpa)	STDEV	<i>H</i> (Gpa)	STDEV	<i>E/H</i>	<i>E</i> (Gpa)	STDEV	<i>H</i> (Gpa)	STDEV	<i>E/H</i>
1	50.35	2.65	2.56	0.16	19.66	49.46	3.98	2.67	0.19	18.52	68.78	3.39	3.20	0.12	21.46
10	51.35	3.27	2.62	0.26	19.59	51.12	1.84	2.71	0.04	18.86	65.42	3.12	3.50	0.22	18.66
15	53.22	1.23	2.82	0.02	18.87	53.72	1.63	2.86	0.02	18.78	67.88	1.33	3.94	0.11	17.22
25	69.34	5.76	3.63	0.3	19.10	72.21	1.76	4.12	0.26	17.52	69.22	1.44	4.43	0.13	15.62

Table 3.1. In-situ nanoindentation results at various strain rates.

Chapter 4

MODELING OF INDENTATION IMPACT ENERGY MODEL

Contents

4.1	Development of Indentation Impact Energy Model	74
4.1.1.	Introduction	
4.1.2.	Indentation Impact Energy Model	

4.1. Development of Indentation Impact Energy Model

4.1.1 Introduction

Though previous dynamic indentation testing results had little physical meaning, i.e. estimation of fracture characteristics, research using the dynamic indentation method to define fracture characteristics continued. However, the limited repeatability of the dynamic indentation result restricted improvement of the method to interpret the dynamic indentation property. Similarly, concerned attempts are ceased to just analyzing fracture phenomenon of nano-scale brittle feature using dynamic indentation testing which lacks a standard test method, i.e. thin-film delamination [93]. For metallic materials, previous assessments are limited because indentation crack formation is restricted by the ductility of material.

Given the advantages of indentation testing in determining localized properties is still required in metallic structural components due to limitations in formation of testing specimen. However, application of previous crack based approaches to metallic materials basically requires several conditions of crack generation. The present study overcomes the limitations of previous approaches by development of indentation impact energy model for the newly designed dynamic indentation system. The

developed testing device is designed to undergo large impulse loading and record the data precisely and quickly in order to handle crack-generating conditions in metallic materials.

Generation of an indentation crack in the model is explained by assumption of imaginary crack formation induced by the acceleration of crack nucleation with dislocation pile-up in the slip plane from the dynamic deformation [65]. The interpretation of energy from the indentation impact load-displacement curve with crack formation is based in Johnson's research on indentation cracking [56]. The research interprets indentation-induced crack with a change in the plastic zone expansion rate beneath the indenter during indentation. Here we modify the concept of plastic zone expansion rate with indentation strain rate of Doerner and Nix [1]. The indentation impact energy of indentation impact energy model has a close relation with the absorbed energy of CVN testing.

4.1.2. Indentation Impact Energy Model

4.1.2.1. Basic concept

The Charpy V-notch impact test (CVN test) is a generally used method to assess the impact fracture property of metallic structural components. Since CVN energy is the result of the CVN test, the present study focused on estimating the indentation impact absorbed energy corresponding to the CVN energy. The basic modeling concept focuses on the similarities between the CVN test and indentation impact test:

-Both tests inflict dynamic fracture on the material.

: Both tests use a dynamic strain rate ($10^2 \sim 10^6/s$), indentation impact ($\sim 10^3/s$) and CVN impact ($\sim 10^6/s$)

- The tests have similar stress distributions (beneath the indenter and the V notch) because of their geometrically similar shape

- The tests have similar crack formation processes: crack initiation, enlargement, and propagation

A stress analysis of notched bar bending shows similar stress distributions with sharp indentation [29]. The penetration of a sharp tip that

is geometrically self-similar can be considered as the opening of a notch, though the tests have different loading mechanisms. The similarity of stress distribution is discussed as the result of similar geometry between a V notch and a sharp indenter tip. Finite element analysis of CVN testing and indentation [58] also shows similarities in distributed stress.

Using these similarities, the present model focuses on defining the energy absorbed during indentation impact process, since it may show trends similar to CVN energy. Then the CVN energy is estimated using the newly defined indentation impact energy.

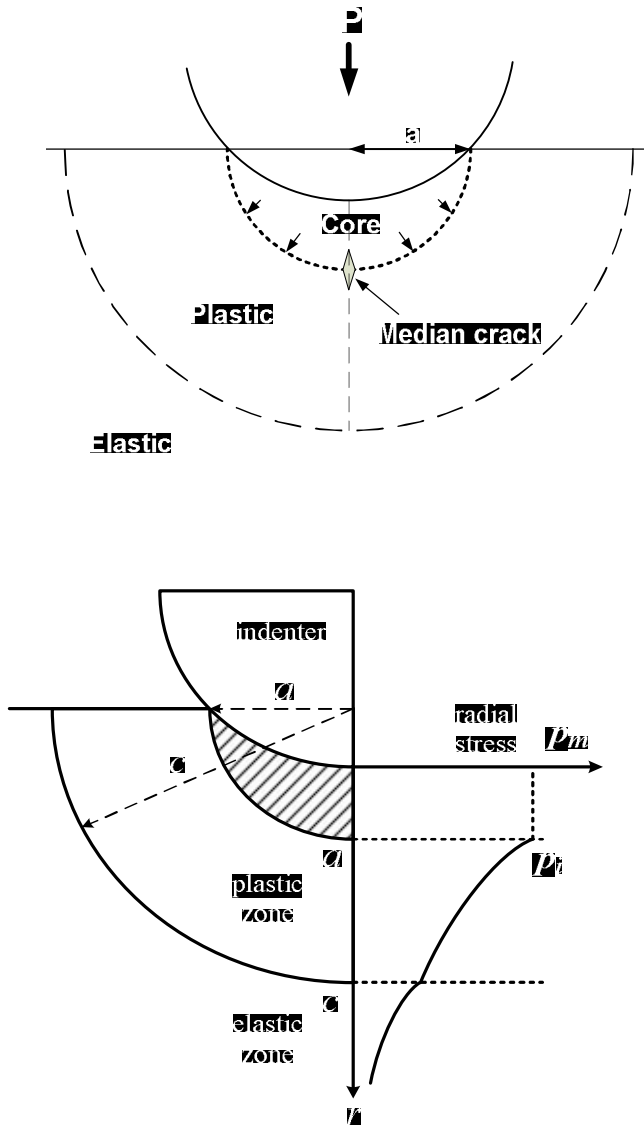


Figure 4.1. Distribution of radial stress of indentation along the z -axis.

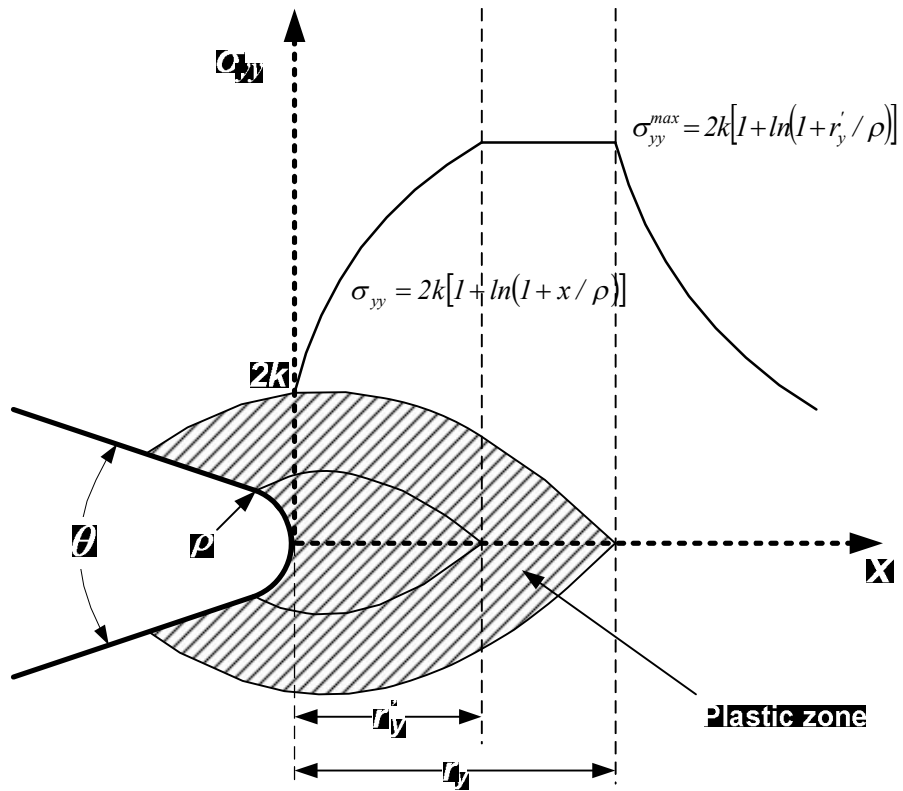


Figure 4.2. Schematic longitudinal stress distribution ahead of a rounded notch at general yielding: rigid plastic slip-line field solution

4.1.2.2. Fracture Criterion in the Indentation Impact Energy Model

The generation of indentation-induced crack is essential in defining an energy model of indentation impact fracture, previous approaches to indentation cracking are limited in application to metallic materials due to their ductility, since the fracture strength of metallic materials is relatively greater than that of brittle materials. For sharp indentations, it is known that maximum tensile stress beneath the indenter depends only on indenter angle. The maximum stress can be calculated using the expanding-cavity theory of Gao [51].

Using the stress distribution in the deformed region, Johannis [60] calculated the value of maximum tensile stress as nearly half the material yield stress. This result showed that for general metallic materials, cracking does not occur even with increases in indentation loading. It is generally known that indentation cracking does not occur in sharp indentations even in metals showing brittle behavior in standard impact tests. However, indentation cracking is a precondition to correlating indentation impact energy with CVN energy, since CVN energy is defined as energy absorbed during impact fracture.

In a microscopic view of the fracture process, fracture is initiated by the formation of a micro-crack. According to Johanns' indentation-induced fracture model, micro-cracks initiate from flaws, either pre-existing or induced by deformation. Deformation-induced flaws tend to nucleate at points of intense stress concentration ahead of locally impeded dislocation bands or zones of inelastically deformed material [29]. Theories of micro-mechanisms of deformation-induced flaws involve dislocation pile-up at intersecting slip planes [65].

Lloyd [100] proved formation of indentation-induced flaws due to dislocation pile-up at intersecting slip planes with the cross-sectional trace of nano indentation in TEM analysis. For a sharp indenter, a deformation-induced flaw develops into a small crack on a plane of symmetry containing the contact axis. An increase in the loading causes this median crack to grow, as in Fig. 4.4. However, deformation-induced flaws are unlikely to appear under general indentation conditions of metallic materials. In the present model, generation of deformation induced flaws are assumed due to extremely rapid deformation with the dynamic indentation test as deformation-induced flaws could be explained in the case of accelerated work hardening.

As the testing time of indentation impact test is extremely short, 0.5ms, it was impossible to apply the previous crack detecting method such as

ultrasonic device to determine the flaw generation. And also, the generated flaw could not be found easily with the crosscut of the indented area due to its location, underneath the indented area, and the size of flaw which is in nanometer scale. Thus, imaginary crack formation is assumed from the unique appearance of surface traces of indentation impact which could explain the deformation induced crack formation.

With the indentation impact test, massive amounts of pile-up compared with static indentation are found with the indentation impact imprints in Fig. 4.5, though the final depth of the indentation impact is about 100 μm or less.

This could be the evidence for appearance of rapid deformation-induced dynamic work hardening with maximized dislocation movement and pile-up at intersecting slip planes. Then the flaw initiated at the point of maximum tensile stress beneath the indenter overcomes the fracture stress.

And also, crack-like features were also found with the indentation impact of a Vickers indenter in Fig. 4.6. As crack initiation in indentation impact test is proven, indentation energy with crack formation can be defined with indentation impact test.

Johanns interpreted indentation fracture in crack growth in three steps: 1) flaw initiation, 2) crack enlargement, 3) crack propagation; CVN fracture is also explained in the same manner. The indentation impact energy corresponding to CVN energy can be determined by summation of the

defined energies of each cracking step.

Since indentation energy is defined as the area of the indentation load displacement curve, the impact energy of each step in crack growth can be calculated by integration at each crack growth step. Thus a criterion for defining crack growth steps during indentation cracking is essential. However, the generally used load criterion explaining the state of crack growth is useless because indentation load increases continuously due to compressive indentation loading, even though a crack has formed [60].

Thus, a criterion using the plastic zone expansion rate is taken from previous research to define steps of indentation crack growth during indentation impact test. Puttick et al [59] investigated the relation of indentation pressure and fracture pattern for polymethyl methacrylate (PMMA) assuming an ideally plastic material using simple plastic-elastic models of the strain field such as Hill and Johnson's cavity model [57,58]. In their research, the effective rate of cavity expansion is equal to the constant penetration rate of indenter when indentation reaches critical condition of crack formation:

$$\text{Rate of Expansion} = \frac{\text{Final plastic zone size}}{\text{time}} = \frac{dc}{dt} \quad (4-1)$$

$$\frac{dc}{dt} = \frac{v}{a} = \text{constant (v: rate of penetration)} \quad (4-2)$$

The present indentation impact model expands the approach of plastic zone

expansion rate change to all steps of indentation crack growth. Since the plastic zone expansion rate is a calculated value from the expanding cavity model (ECM) of sharp indentation, a parameter directly gained from indentation testing is needed to define each step in the indentation load-displacement curve. The plastic zone expansion rate calculated by ECM is modified using the strain-rate definition of Doerner and Nix [1].

For a sharp indenter (geometrically self-similar shape, fixed indentation angle), the penetration rate can be expressed using the final radius of indentation per unit time:

$$v(\text{rate of penetration}) \approx C \left(\frac{da}{dt} \right) \quad (C: \text{correlation constant}) \quad (4-3)$$

As the definition of expansion rate is penetration rate divided by contact radius of indenter, the definition can be changed from Eq. (4-3) to Eq. (4-4), where it is a function of indenter radius:

$$\frac{dc}{dt} = \frac{v}{a} \approx C \left(\frac{1}{a} \frac{da}{dt} \right) \quad (4-4)$$

With the definition of indenter radius for sharp indenter (Vickers and Berkovich) [19], the definition of the plastic zone expansion rate can be given a displacement form (4-5):

$$\frac{dc}{dt} = \frac{v}{a} \approx C \left(\frac{1}{a} \frac{da}{dt} \right) \approx K \left(\frac{1}{h} \frac{dh}{dt} \right) \approx \dot{\epsilon} \quad (4-5)$$

It is seen from this modified definition of plastic zone expansion rate that the criterion of plastic zone expansion rate can be replaced by the indentation strain rate change during indentation impact.

Since strain rate is made up of direct parameters of the indentation impact test result (displacement and time), the steps in crack growth in the indentation impact test can be detected directly from the indentation impact test result using a criterion of strain-rate change. With this criterion of strain rate, each step in crack growth can be determined in indentation impact load displacement curve. Thus, the indentation impact energy corresponding to CVN energy can be calculated by the summation of absorbed energy for each crack growth step.

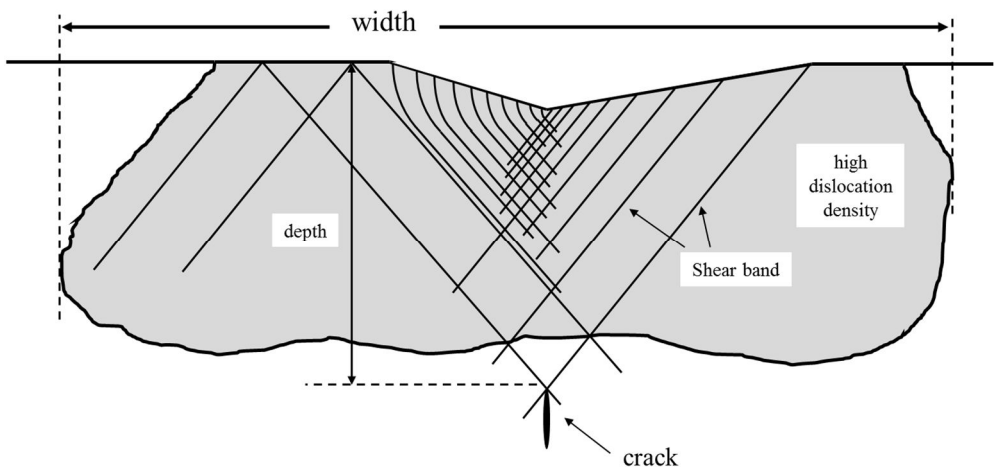
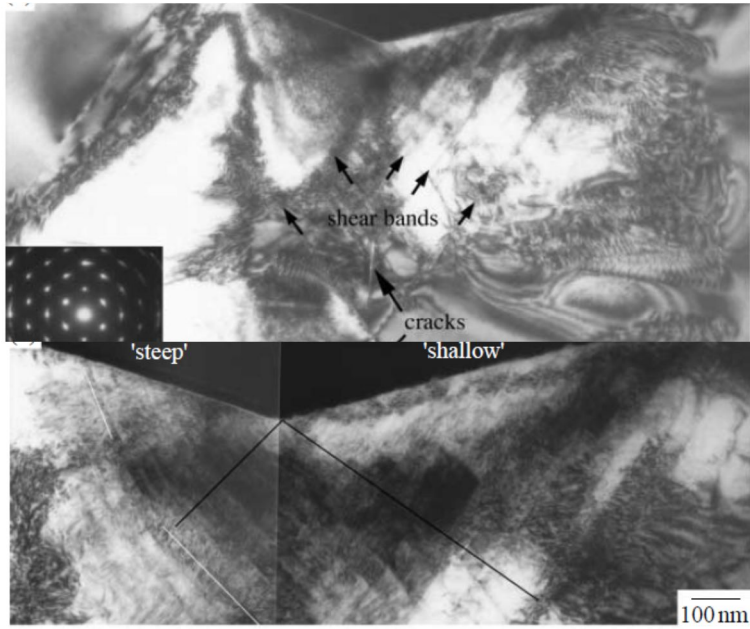


Figure 4.3. TEM analysis of indentation-induced flaw formation from cross-sectional nanoindentation trace [100].

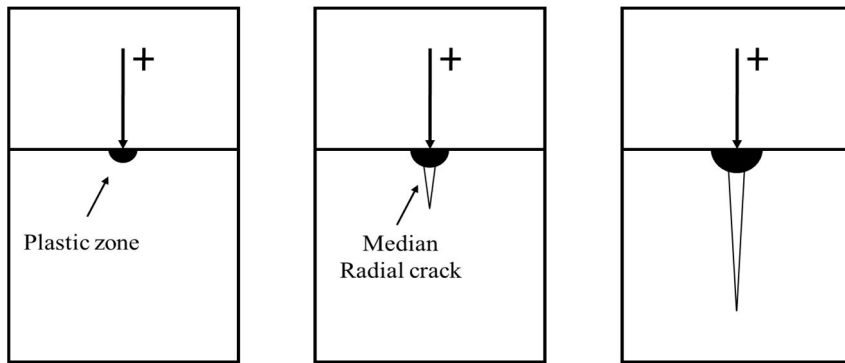


Figure 4.4. Schematic of an ideal vent crack formation beneath point load indentation. Fracture starts from inelastic deformation (dark zone) [29].

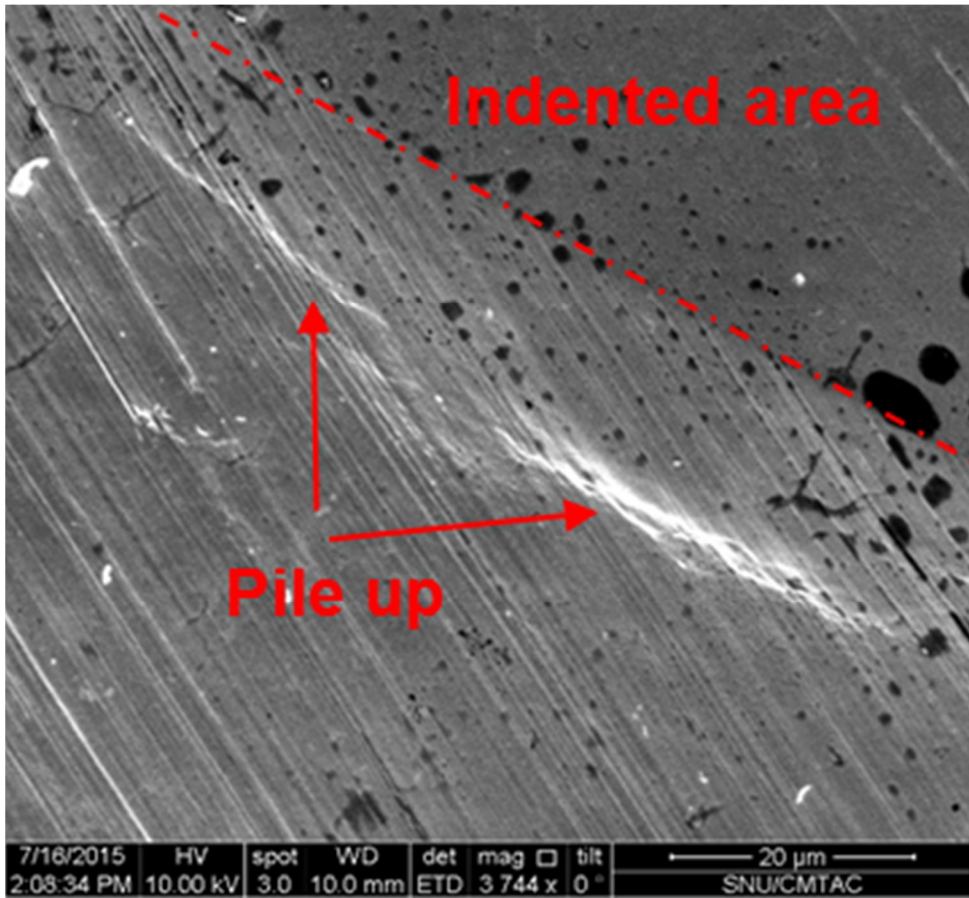


Figure 4.5. Indentation-induced pile-up trace in indentation impact test.

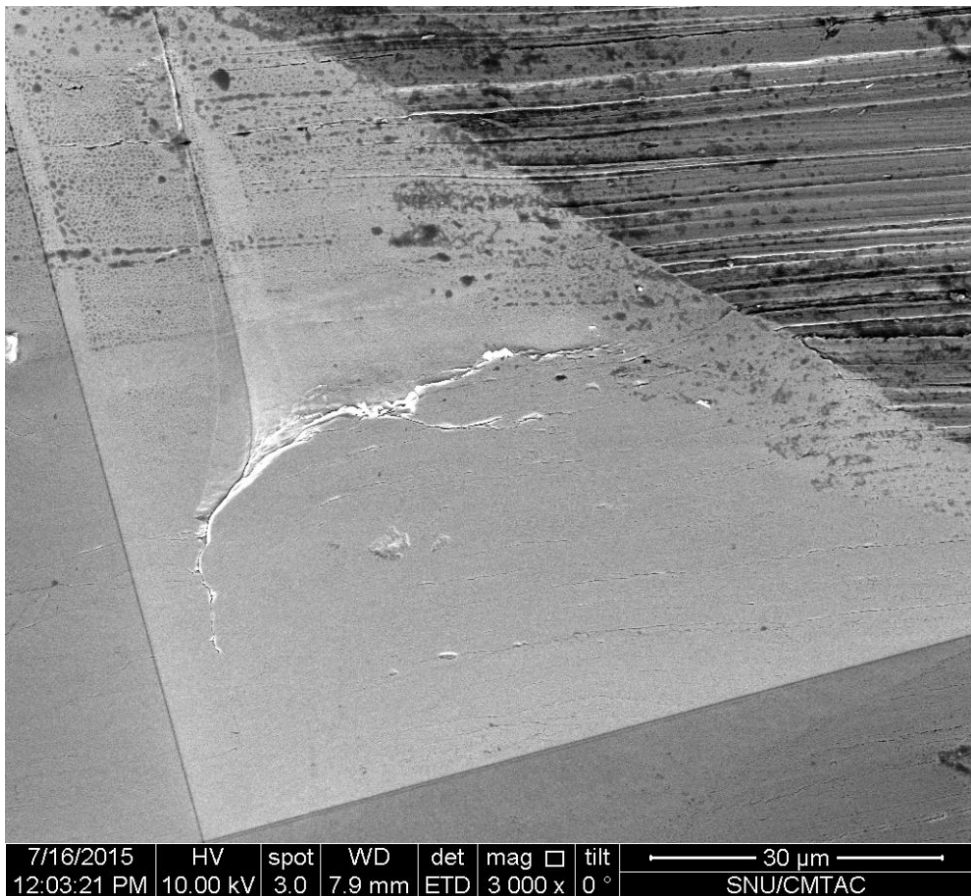


Figure 4.6. Crack-like feature of Vickers indentation impact trace.

3.1.2.2. Indentation Impact Energy Determination Using the Criterion

From the strain-rate criterion defined in the previous section, the absorbed impact energy of indentation impact can be specified by the steps in indentation crack growth. Previous research on sharp indentation defines the strain of indentation by the indenting angle [60]. And the nearly constant indenting velocity in static indentation creates a constant strain rate.

For static indentation with a sharp indenter, the strain rate criterion is difficult to apply because of the nearly constant strain rate. However, change in indentation velocity during indentation impact testing is derived by different impact loading mechanism. The indentation impact test uses controlled potential energy, like other impact tests. First set potential energy is changed into the kinetic energy of indenter, and some part of the kinetic energy is transformed into deformation during indentation impact process. The indentation velocity is affected by the rate of change of deformation, which has the same meaning as the absorbed energy increase rate during indentation impact. Indentation-induced rate of change of deformation can be

expressed in terms of strain rate, as discussed above. Since the rate of change of deformation differs during indentation crack formation, the strain rate can be used as criterion for indentation impact crack formation. Figure 4.7 shows strain rate vs. time in an indentation impact test. The strain rate increases slightly at first and decreases to a constant value. This aspect of the curve can be explained by crack formation during indentation, as shown in Fig. 2.7. Aspects of the strain rate time curve match with the three steps of crack formation, flaw initiation, crack enlargement, crack propagation,.

It was mentioned in the previous section that deformation-induced flaws in sharp indentation impact are assumed to be generated from accelerated dislocation pile-up on the slip-plane intersection (dynamic work hardening). The strain rate increases during the indentation impact process due to dynamic work hardening. This can be explained by the concept of absorbed energy increase rate in expanding the plastic zone beneath the indenter. The absorbed energy to expand the plastic zone increases proportionally to the amount of work hardening until a flaw is generated that releases this absorbed energy. At the point of flaw generation, the strain rate, which contains the plastic zone expansion rate, is maximum. This trend appears in the strain rate vs. time curve of indentation impact in Fig. 4.7. The time of maximum strain rate, t_1 , can be determined from Fig. 4.7. At t_1 , a deformation-induced flaw initiated. As the displacement h_{t1} at t_1 can be

defined from the displacement-time curve, the absorbed impact energy to flaw initiation, i.e. the energy for step 1 of indentation crack growth, can be obtained as the area beneath the load-displacement curve until h_{t1} :

$$\text{Absorbed impact energy to flaw initiation}(E_{Ii}) = \int_0^{h_{t1}} f(h)dh \quad (4-6)$$

Continuous loading induces the initiated flaw to form a crack. The generation of short crack regime is called crack enlargement, indentation crack growth (step 2) by Johannis [60]. As the indentation impact test is controlled by potential energy, like other impact test methods, the potential energy applied by the indenter impact is fixed; some of this energy is used for deformation and some is released by crack formation.

After flaw initiation, the absorbed energy increase rate to expand the plastic zone beneath the indenter decreases with crack enlargement. This is shown in the indentation strain rate vs. time curve in Fig. 4.7: strain rate decreases from its maximum value and become constant. The time of crack enlargement can be defined as the time of stabilization, which is the time between flaw initiation (t_1) and crack propagation (t_2). Thus, the impact energy absorbed during crack enlargement, which is the energy for step 2 of indentation crack growth, can be obtained as the area of the load-displacement curve from h_{t1} to h_{t2} :

$$\text{Absorbed impact energy during crack enlargement } (E_{Ei}) = \int_{h_{t1}}^{h_{t2}} f(h)dh \quad (4-7)$$

In Griffith's theory, the two important factors in fracture are 1) crack initiation and 2) crack propagation. Of the two, crack initiation is how and where a crack starts. Thus crack initiation contains flaw initiation and crack enlargement. The summation of calculated energy E_{Ii} and E_{Ei} is the crack initiation energy of indentation impact fracture.

Indentation is a localized test of bulk material and does not induce specimen failure, so that the crack propagation of indentation is not restricted by specimen failure. From Johannis[60], crack propagation of indentation can be regarded as steady-state crack growth. And Puttick's[59] investigation of the constant plastic zone expansion rate during crack formation can also be explained in this manner. Since indentation impact is also a localized test of bulk material and does not induce specimen failure, crack propagation can be regarded as steady-state crack growth that might be faster than in static indentation. Due to steady-state crack growth, the rate of energy release during crack propagation is constant. This causes the rate of increase in absorbed energy in expanding plastic zone to be constant during crack propagation. It is also shown in strain rate vs. time curve in Fig 4.7 that crack propagation starts at t_2 when the strain rate becomes constant. Thus, the absorbed impact energy during crack propagation, which is the energy for

step 3 of indentation crack growth, can be obtained as the area of load-displacement curve from h_{t2} to h_{te} :

$$\text{Absorbed impact energy during crack propagation } (E_{Pi}) = \int_{h_{t2}}^{h_{te}} f(h)dh \quad (4-8)$$

Indentation impact energy including crack formation can be calculated as the sum of the absorbed energy in each step:

$$\begin{aligned} \text{Indentation Impact energy } (E_I) \\ = \int_0^{h_{t1}} f(h)dh + \int_{h_{t1}}^{h_{t2}} f(h)dh + \int_{h_{t2}}^{h_{te}} f(h)dh \end{aligned}$$

However, as mentioned above, indentation is localized test of bulk material and does not induce specimen failure, unlike CVN testing. CVN energy is also known to be affected by specimen geometry. Though indentation impact energy is defined from a similar geometry, the stress distribution of energy controlled test, it differs from the specimen geometry that can induce errors in estimating CVN energy from the indentation-based impact energy.

CVN test – specimen geometry is defined by standard

Indentation impact test – regarded as miniaturized CVN test on bulk material

The error could be compensated for by defining a absorbed energy during crack propagation corresponding to CVN energy because specimen geometry has major influence on the end point of the fracture: the energy of first two

steps of fracture is regarded as mainly influenced by pre-assumed similarities (notch geometry and stress distribution).

As indentation impact test is regarded as a miniaturized CVN test with bulk material, the energy absorbed in crack propagation is defined by the indentation impact testing time condition only (the propagation time defined from t_2 to t_{pe} , the test end time). Thus, the energy absorbed during crack propagation is redefined from the basic model assumption to correlate with the CVN energy of crack propagation.

From the basic concept of the indentation impact energy model, we assumed that Charpy V-notch impact energy (CVN energy) has a close relationship to indentation impact energy (II energy).

- Both test inflict dynamic fracture
- Similar stress distributions underneath the indenter and V notch because of geometrically similar shape
- Similar crack formation: Crack initiation, enlargement, propagation

Due to this close relationship, the II energy with crack propagation corresponding to CVN energy with crack propagation can be determined by interpreting the relationship between CVN energy and II energy.

From the similarity-based close relationship between CVN energy and II energy, we can imagine II test as a miniaturized CVN test with a relatively thick specimen that does not fail. Then the same linear relation of energy absorbed with each crack growth step can be assumed if the corresponding II energy of crack propagation is defined:

$$CVN = KE_i \quad (4-10)$$

$$CVN_I : CVN_E : CVN_P = KE_{Ii} : KE_{Ei} : KE_{Pi} \quad (4-11)$$

Thus, if the II energy during crack propagation (E_{Pi}) is determined, then the value can be correlated with the CVN energy during crack propagation (CVN_p):

$$CVN_P = KE_{Pi} \quad (4-12)$$

The constant K is a correlation factor between CVN energy and II energy.

Then the rate of absorbed energy increase during crack propagation should have a linear relation in both tests if the relation of E_{Pi} and CVN_p is established. Figure 4.9(b) shows the absorbed energy vs. time curve in CVN and II. As the absorbed energy increase rate during crack propagation is the slope of Fig.4.9 at crack propagation time, the relation between slopes can be

$$\frac{CVN_P}{t_{Pc}} = S \frac{E_{Pi}}{t_{Pi}} \quad (4-13)$$

The constant S is a correlation factor between absorbed energy increase rates.

In the present model, two assumed relations based on similarities between CVN test and II test are used to obtain the II energy corresponding to crack propagation (E_{Pi}) from the II energy during crack propagation until test ends (E_{Pe}). To determine E_{Pi} from the results of the indentation impact test, which has no specimen failure, the energy term with crack propagation independent of experimental conditions must be extracted. From the indentation impact test results the II energy during crack propagation until the test ends (E_{Pe}) and crack propagation time until the test ends (t_{Pe}) are obtained.

As indentation impact-induced crack propagation is regarded as steady-state crack growth in the previous section, the rate of absorbed energy increase during crack propagation state is constant. In Fig. 4.10, showing indentation impact energy vs. time, the crack propagation state has constant slope.

Because of the constant rate of absorbed energy increase during crack propagation, the absorbed energy increase rate to t_{Pe} can have the same value as the absorbed energy increase rate to crack propagation time of E_{Pi} . Thus, the absorbed energy increase rate to t_{Pe} can be regarded as an energy term independent of test conditions. And the relation between E_{Pe} and I_{Pi} is obtained as

$$\frac{E_{Pe}}{t_{Pe}} = \frac{E_{Pi}}{t_{Pi}} \quad (4-14)$$

E_{Pi} is calculated by combining the following two relations:

- Relation between CVN_P and E_{Pi} assumed based on similarity

$$CVN_P = KE_{Pi} \quad (4-12) \qquad \frac{CVN_P}{t_{Pc}} = S \frac{E_{Pi}}{t_{Pi}} \quad (4-13)$$

- Relation between E_{Pi} and E_{Pe} assumed with indentation crack growth

$$\frac{E_{Pe}}{t_{Pe}} = \frac{E_{Pi}}{t_{Pi}} \quad (4-14)$$

$$CVN_P = t_{Pc} S \left(\frac{E_{Pi}}{t_{Pi}} \right) \quad (4-15)$$

$$CVN_P = KE_{Pi} \quad (4-12)$$

$$KE_{Pi} = t_{Pc} S \left(\frac{E_{Pi}}{t_{Pi}} \right) \quad (4-16)$$

$$E_{Pi} = t_{Pc} \frac{S}{K} \left(\frac{E_{Pi}}{t_{Pi}} \right) \quad (4-17)$$

$$\frac{E_{Pe}}{t_{Pe}} = \frac{E_{Pi}}{t_{Pi}} \quad (4-13)$$

$$E_{Pi} = t_{Pc} \frac{S}{K} \left(\frac{E_{Pe}}{t_{Pe}} \right) \quad (4-18)$$

The calculated E_{Pi} is made up of the constant K , S , t_{Pc} , and the increase absorbed energy rate during crack propagation until the test ends.

As mentioned above, the constant K is a correlation factor between CVN energy and II energy, and can be regarded the ratio of absorbed energy

between CVN test and II test. Thus K can be calculated as the ratio of the deformed volumes;

$$K = \frac{CVN_P}{E_{Pi}} = \frac{CVN}{E_i} \approx \frac{\text{CVN plane strain plastic zone volume (Fracture mechanics)}}{\text{Indentation plastic zone volume (Expanding Cavity model of sharp indentation)}} \quad (4-19)$$

The deformed volume in CVN testing is calculated from the definition of the plastic zone radius in fracture mechanics written by T.L. Anderson. For indentation impact testing, the expanding cavity model of Gao [51] is applied. In results on 14 metallic materials used for model construction, K was $1.5 * 10^3$. Though both equations for calculating volume contain many assumptions, the calculated K should be re-discussed with K value from the final result: the relation of CVN energy and calculated II energy from the indentation impact energy model. The error in K is handled by iteration from the K value of the final result. The compensated K value was $1.968 * 10^3$.

The constant S is a correlation factor for the rate of absorbed energy increase during crack propagation between the CVN and II tests. As the rate of change in deformation is taken as the rate of change in absorbed energy in the previous section, the constant S can be the same as the strain rate ratio S estimated by the strain rate difference between the two tests. The value of the constant S turns out to be 10^3 :

$$S = \frac{CVN_P/t_{pc}}{E_{Pi}/t_{pi}} = \frac{CVN \text{ strain rate } : \sim 10^6}{\text{Indentation impact strain rate } : \sim 10^3} \approx 10^3 \quad (4-20)$$

With the above definition of each parameter, the formation of absorbed indentation impact energy during crack propagation could be defined by the indentation parameters and t_{pc} , the crack propagation time in the CVN test. As t_{pc} contains the ductility, it is treated in the next section.

$$E_{pi} = t_{pc} \frac{S}{K} \left(\frac{E_{pe}}{t_{pe}} \right) = t_{pc} \times \frac{S(\text{strain rate ratio} \sim 10^3)}{K(\text{deformed volume ratio} \sim 1.76 \times 10^3)} \left(\frac{E_{pe}}{t_{pe}} \right) = 0.51 t_{pc} \left(\frac{E_{pe}}{t_{pe}} \right) \quad (4-21)$$

The final form of the indentation impact energy corresponding to CVN energy is:

$$\begin{aligned} \text{Indentation impact energy } (E_I) \\ = \int^{h_{t1}} f(h) dh + \int^{h_{t2}} f(h) dh + 0.51 t_{pc} \left(\frac{E_{pe}}{t_{pe}} \right) \end{aligned} \quad (4-21)$$

4.1.2.3. Modeling Based on Ductility

It is essential to explain the value of t_{pc} in order to define the final form of indentation impact energy using only indentation parameters. From previous research, the failure time in a CVN test is considered similar for materials with same fracture mechanism. François [98] states that the reason for the similar values is the high velocity (5.2 m/s) of the CVN test. Due to this high velocity, the influence of material property on failure time is small

if the fracture mechanism is similar. We can suppose that crack propagation time has the same tendency if the materials experience similar fracture mechanism. Thus, t_{pc} contains meaning of ductility because it is related to the fracture mechanism of the material. It can be regarded as an almost constant value for materials showing the same fracture mechanism because of the high velocity of CVN testing, even though t_{pc} is a material-dependent parameter. CVN failure time and crack propagation time with different fracture mechanism are [98]:

- Lower shelf (brittle) : ~ 0.06 ms (with no energy of crack propagation)
- Transition : ~ 2 ms (crack propagation time ~ 1 ms)
- Upper shelf (ductile) : ~ 6 ms (crack propagation time ~ 3 ms)

The value of t_{pc} from the above result [98] is experimentally determined from the instrumented CVN test value. For model constructions, time constant of ductility C is defined from the expected value of averaged t_{pc} ; averaged t_{pc} could be regarded as constant because scatter is relatively small among materials showing same fracture mechanism.

Defined value of averaged t_{pc} is determined by FEA simulation using ANSYS. FEA simulation using ANSYS showed similar results for t_{pc} as a previous study [98]. The average value of t_{pc} for seven kinds of ductile materials calculated as 3.6 ms. Then the average t_{pc} value for materials on

transition is estimated as 1.2 ms since it is taken as 1/3 of t_{pe} of ductile materials in the above research. Thus the ductility constant C is applied to the definition of indentation impact energy:

$$\text{indentation impact energy } (E_I) = \int_0^{h_{t1}} f(h)dh + \int_{h_{t1}}^{h_{t2}} f(h)dh + 0.51C \left(\frac{E_{Pe}}{t_{Pe}} \right)$$

(Upper shelf : $C=3.6\text{ms}$, transition : $C=1.2\text{ms}$, Lower shelf : $C=0$) (4-22)

Because the present indentation impact model varies with material ductility, predetermination of ductility is necessary to improve its application. As mentioned above, the indentation impact test is a controlled potential energy test, like the CVN test. Different load-displacement curves would be found with different material ductilities:

- Brittle material → relatively small indent
- Transition material → average indent
- Ductile material → relatively large indent

From the difference in the load displacement curve, the ductility can be defined as the energy absorbed with crack initiation (flaw initiation and crack enlargement), which can be calculated regardless of model determination.

The possibility of predetermination of ductility from crack initiation energy arises from previous attempts to correlate CVN energy and fracture toughness. As the meaning of fracture toughness is resistance to crack opening, crack initiation energy, which is energy absorbed in crack opening,

can be related to CVN energy. The linear relation shown in Fig. 4.14 is found from the indentation impact test results. And previous research has correlated a distributed model of fracture toughness with material ductility as defined by CVN energy value at transition temperatures [64], nil ductility temperature (NDT) and fracture-transition plastic temperature (FTP). Thus, the criterion of ductility with transition temperature can be used and transformed into an absorbed energy value using the relation of CVN energy and absorbed energy until crack initiation.

From the meaning of each transition temperature, a material is considered brittle when its CVN energy is below 27 J and ductile when its CVN energy is over 60 J (the NDT is the temperature below which the fracture is 100% cleavage/shear). For the CVN test, NDT is defined as the temperature of 28 J CVN energy. FTP is the temperature when the fracture appearance 100% fibrous and is defined as the temperature of 60 J CVN energy.

The value of absorbed energy until crack initiation is calculated as 0.0272 J from the CVN energy (27 J) of NDT and used as brittle criterion. And the value of absorbed energy of the ductile criterion is calculated as 0.0428 from the CVN energy (60 J) of FTP. Then a material is considered brittle when the energy value until crack initiation is less than 0.0272 J. Then the constant C becomes 0. With an energy value between 0.0272 J and 0.0428 J, a material can be considered a transition material and the constant C becomes 1.2 ms.

With energy value greater than 0.0428 J, a material can be considered ductile and the constant C becomes 3.6 ms. Finally, the indentation impact energy model is defined using the ductility criterion. The model as defined is shown in Fig. 4.15. Thus the indentation impact energy corresponding to CVN energy can be calculated.

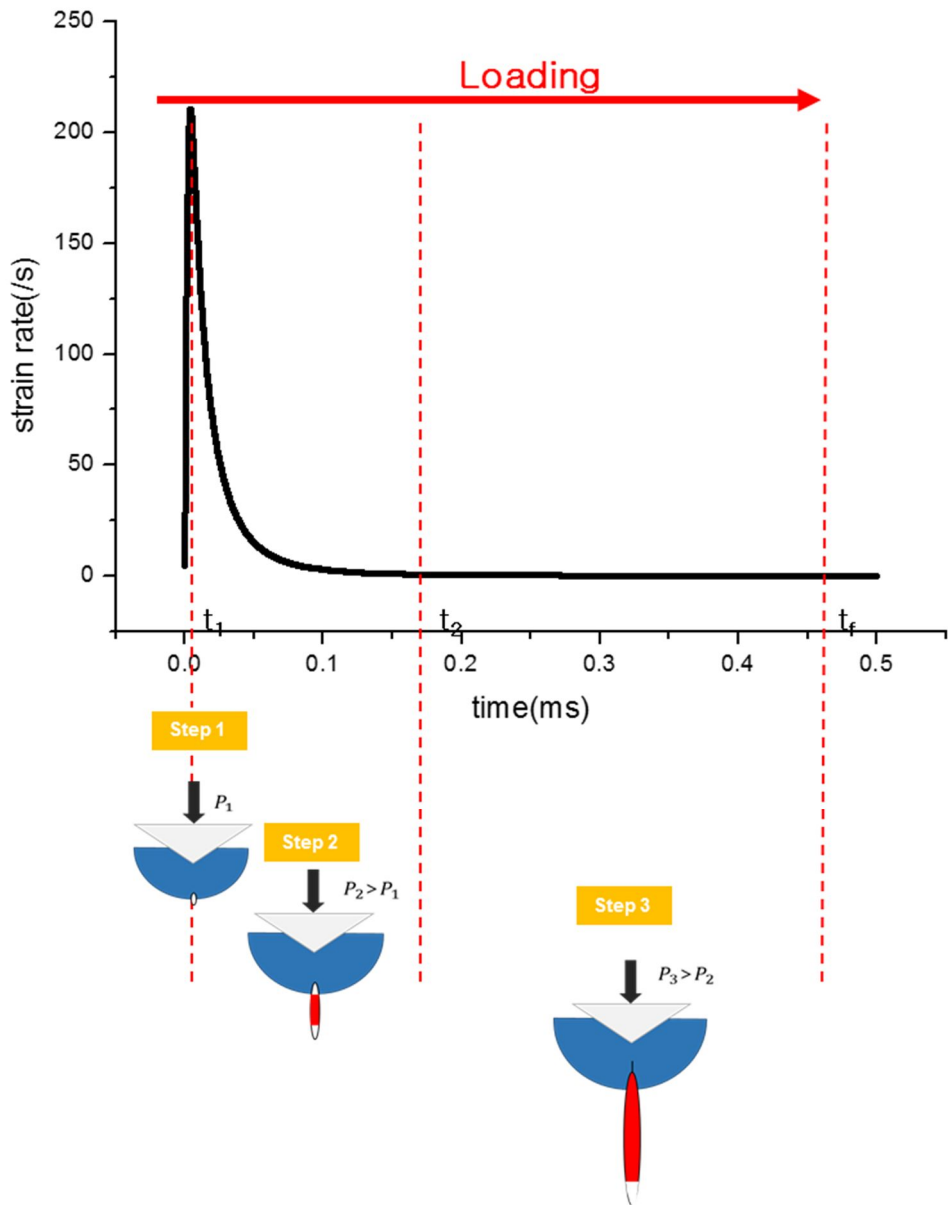


Figure 4.7. Strain rate change during impact loading of indentation impact containing crack formation steps.

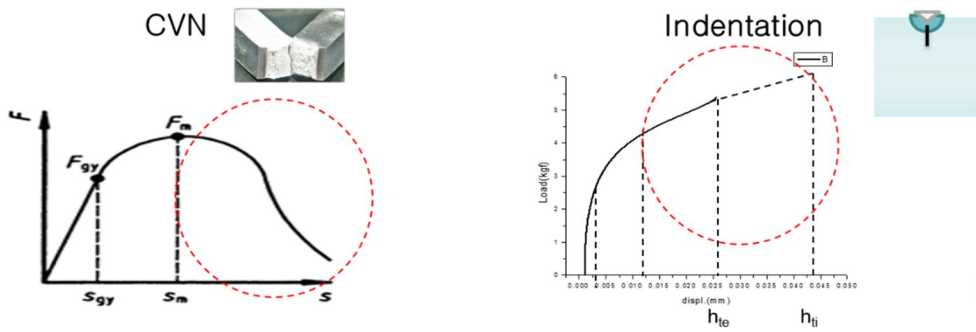


Figure 4.8. Difference in absorbed energy during crack propagation due to specimen failure in CVN test.

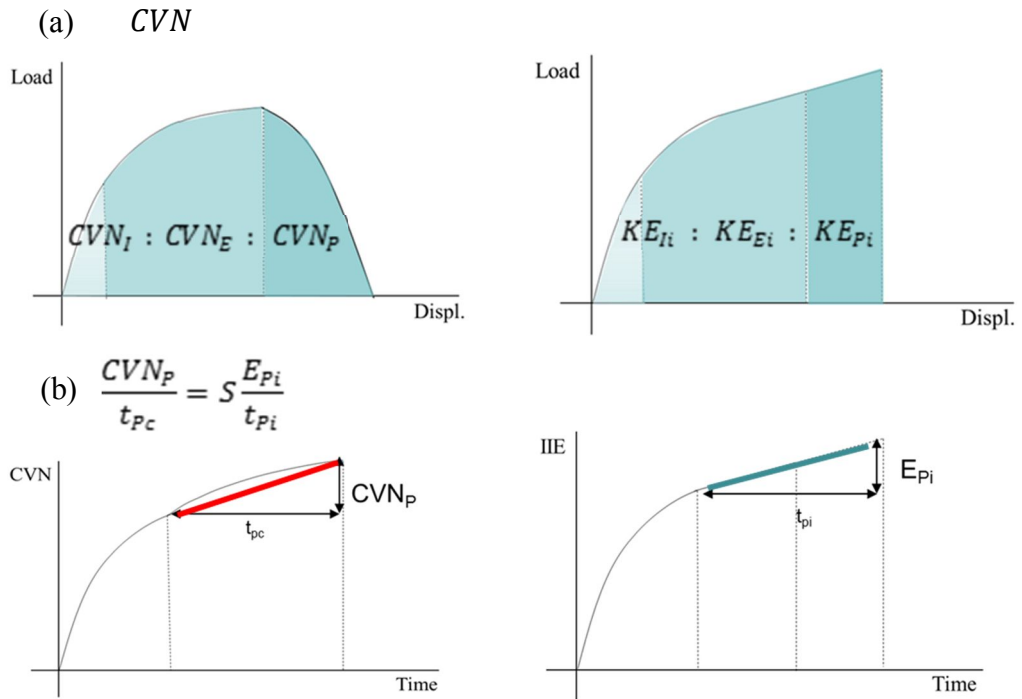


Figure 4.9. Relation between CVN energy and indentation impact energy due to assumed similarities: linear relation of (a) absorbed energy and (b) rate of absorbed energy increase

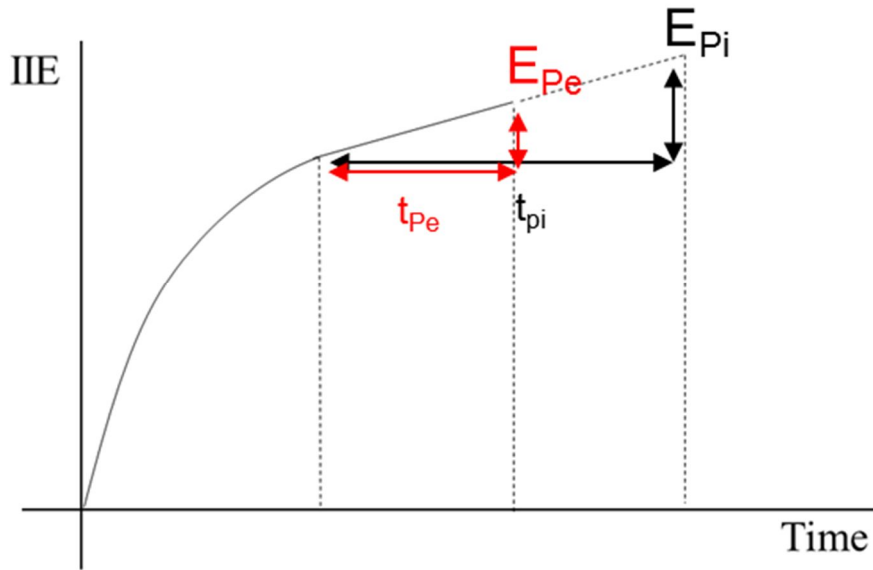


Figure 4.10. Constant rate of absorbed energy increase of indentation impact during crack propagation.

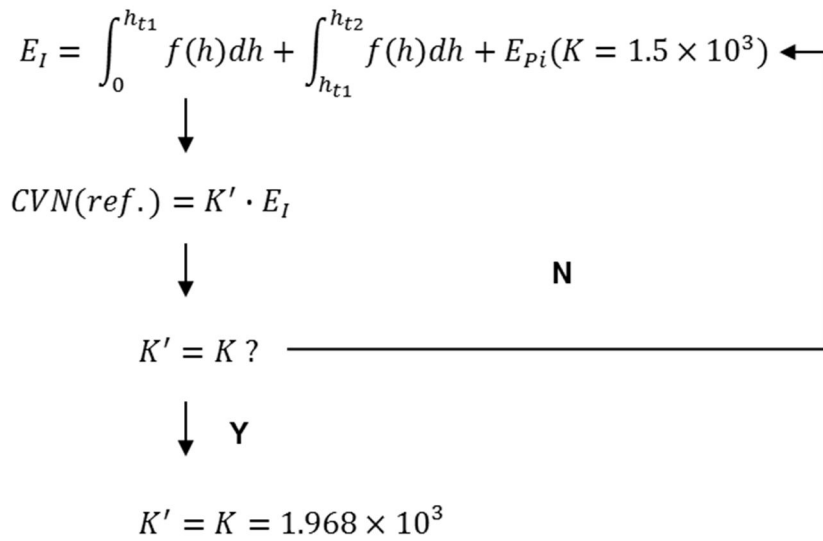


Figure 4.11. Iteration for constant K compensation.

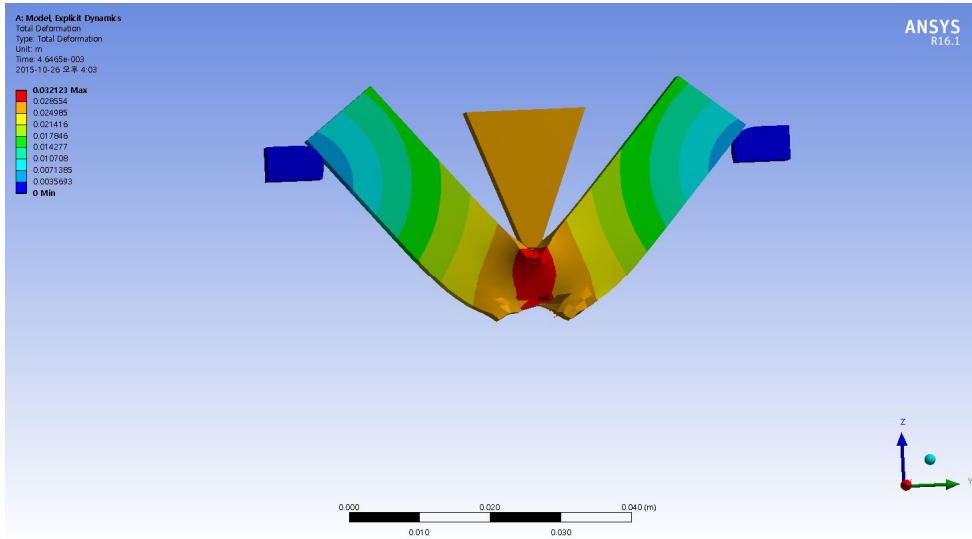


Figure 4.12. FEA simulation of CVN test using ANSYS.

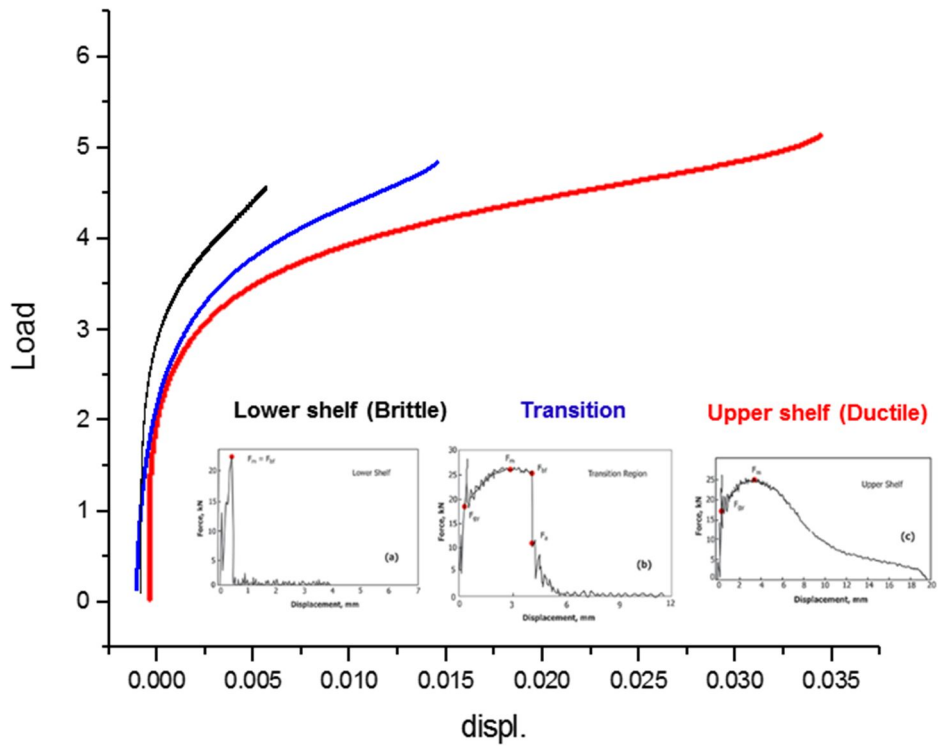


Figure 4.13. Change in load-displacement curve with material ductility.

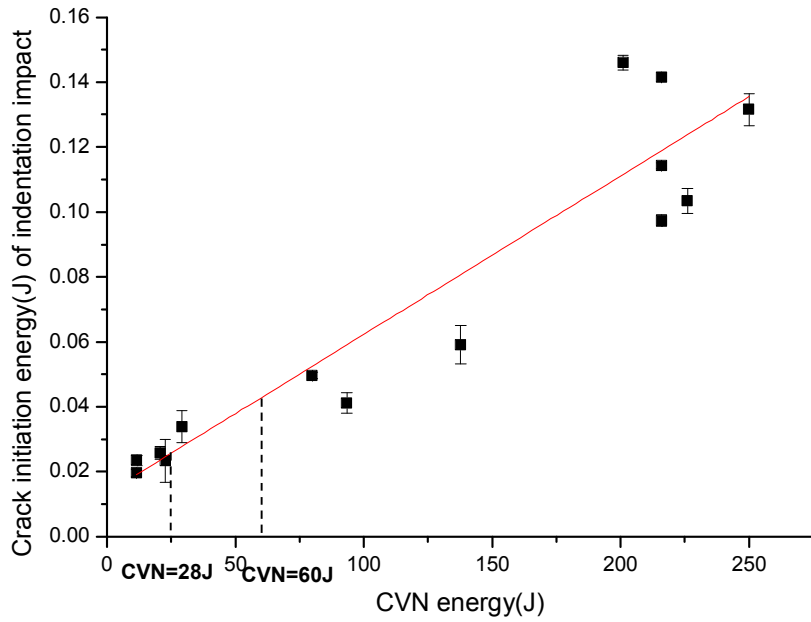


Figure 4.14. Estimate of crack initiation energy criterion based on ductility criterion of CVN energy from transition temperatures [64].

$E_{\text{Crack initiation}} < 0.027\text{J}$ (Meaning of NDT)



$$E_i = \int_0^{h_{t1}} f(h)dh + \int_{h_{t1}}^{h_{t2}} f(h)dh$$

$E_{\text{Crack initiation}} > 0.0428\text{J}$ (Meaning of FTP)



$$E_i = \int_0^{h_{t1}} f(h)dh + \int_{h_{t1}}^{h_{t2}} f(h)dh + \frac{1.83(= 0.51 * 3.6)}{(t_e - t_2)} \int_{h_{t2}}^{h_{te}} f(h)dh$$

$0.027\text{J} < E_{\text{Crack initiation}} < 0.0428\text{J}$



$$E_i = \int_0^{h_{t1}} f(h)dh + \int_{h_{t1}}^{h_{t2}} f(h)dh + \frac{0.61(= 0.51 * 1.2)}{(t_e - t_2)} \int_{h_{t2}}^{h_{te}} f(h)dh$$

Figure 4.15. Steps in indentation impact energy model with ductility criterion.

Chapter 5

MODEL VERIFICATION

Contents

5.1. Experimental Details	113
.....	
5.2. Results and Discussion	119
.....	
5.2.1. Determination of Indentation Impact Energy	
5.2.2. Comparison of CVN Energy Measured in Indentation Impact and CVN Tests	

5.1. Experimental Details

To verify the proposed indentation impact energy model, CVN and indentation impact tests were performed for the different materials listed in Table 4.1. The materials used for this experimental verification were selected according to the industrial requirements for CVN impact energy. (For example, low-alloy Cr-Mo steels are used in power plant facilities.) In addition, various structural steels and tool steels were used for indentation impact tests.

Indentation impact tests were performed with the lab-type indentation impact system in Fig. 5.1. This equipment measured the real-time indentation impact load and depth with impact time through a load cell and a linear variable displacement transducer. The indenter was a tungsten carbide Vickers indenter.

Solenoid energy controlled the impacting loading time of 50 ms. Six sets of indentation impact data were obtained from indentation impact tests for each material, and the average value was used in analyzing the indentation impact energy. Indentation specimens were $20 \times 20 \times 20$ mm and surfaces were polished with $1 \mu\text{m}$ Al_2O_3 powder. The CVN tests were performed according to ASTM E23 [2]. TINUS OLSEN TESTING MACHINE Model 892 was used, and specimens were manufactured in the standard size

proposed in ASTM E23.

Table 5.1 List of tested materials.

																			Unit: %	
No		Material	C	Si	Mn	P	S	Cu	Ni	Cr	V	Mo	Nb	Ti	N	Co	Al	Fe	Sn	
1	Carbon steel	SCM4																		
2		SK3	1.05	0.16	0.27	0.01	0.001	0.03	0.02	0.04		0.01								
3		SKH51																		
4		SKD11	1.49	0.21	0.26	0.02	0.002	0.12	0.23	11.3	0.25	0.82								
5		S45C	0.44	0.25	0.75	0.01	0.004	Tr	0.01	0.02										
6		SKD61	0.39	1.00	0.36	0.02	0.005	0.16	0.23	5.11	0.82	1.13								
7		S20C																		
8	Al-alloy	Al6061																		
9	Cr-Mn steel	SA508 Gr.4N KL4	0.20	0.25	0.3				3.5	1.8		0.5								
10		SA508 Gr.4N KL4_Tempered	0.20	0.25	0.3				3.5	1.8		0.5								
11		SA508 Gr.4N KL4_Mn2	0.21	0.26	0.5				3.6	1.9		0.5								
12		SA508 Gr.4N KL4_Mn2_Tempered	0.21	0.26	0.5				3.6	1.9		0.5								
13		SA508 Gr.4N KL4_Cr2	0.21	0.26	0.3				3.6	2.5		0.5								
14		SA508 Gr.4N KL4_Cr2_Tempered	0.21	0.26	0.3				3.6	2.5		0.5								

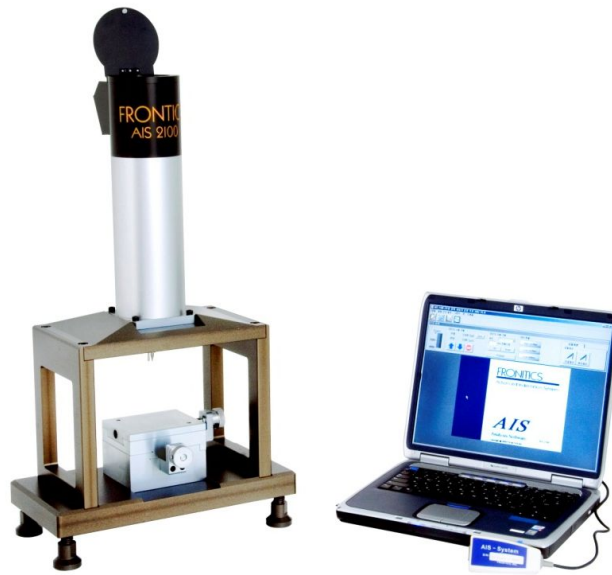


Figure 5.1. Indentation impact system.

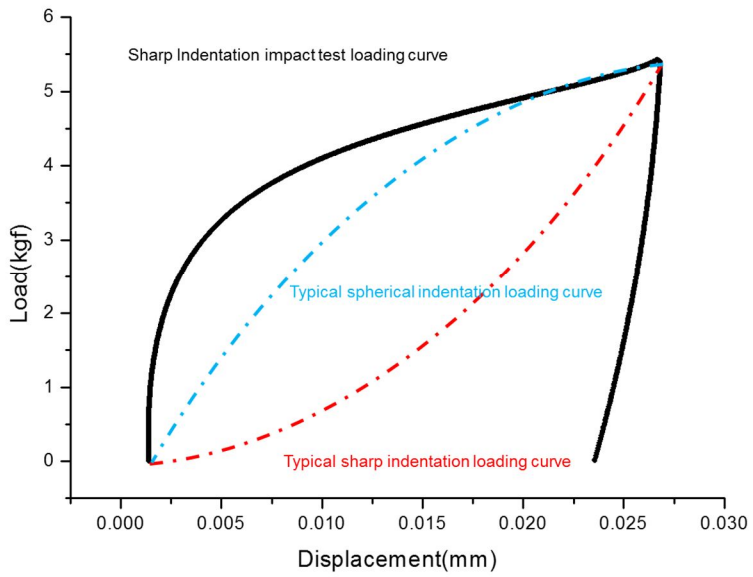


Figure 5.2. Sharp indentation impact loading curve and typical indentation curve.

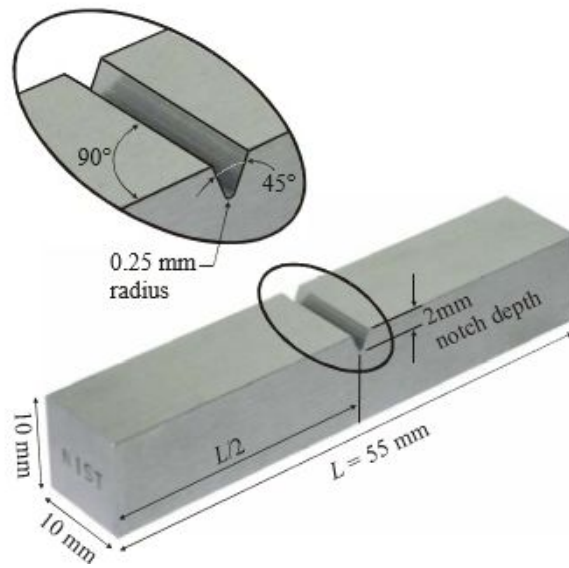


Figure 5.3. Geometry of CVN specimen used in CVN test (ASTM E specification).



Figure 5.4. TINUS OLSEN TESTING MACHINE Model 892 and specimen for CVN tests.

5.2. Results and Discussion

5.2.1. CVN Energy Measured from Indentation Impact and CVN Tests

The values of indentation impact energy obtained from Eq. (4-22) are illustrated in Fig.5.5 and compared with the CVN energy from CVN testing. The defined indentation impact energy of the 14 different metallic materials showed a linear relation with 20% error from the CVN test results. As 20% error is allowed on CVN test results, data points within the 20% error range of CVN data are acceptable.

The correlation equation is defined by linear fitting of the results in Fig. 5.5:

$$\text{CVN(J)} = 1.968 \times 10^3 * E_i(\text{J}) - 29.4109 \quad (5-1)$$

The CVN energy of each material can be correlated with the indentation impact energy using Eq. (5-1). CVN energy estimated from indentation impact energy of carbon steels showed the same low value as reference data for CVN energy. And for Al 6061, whose reference CVN energy lies in the transition area, the estimate was similar. Estimates for Cr-Mo steels were high and the reference CVN energy is also high. The precision of the present

result is confirmed by the correlation of the CVN energy results from both tests shown in Fig. 5.6. A one-to-one relation $y = x$ is seen when the CVN energy estimated from indentation impact testing shows good compatibility with the reference CVN energy. Good compatibility was found, with the result that slope of the data in Fig. 5.6 is almost 1 ($= 0.9992$) and the intercept is almost 0 ($= -0.9623$), nearly a one-to-one relation.

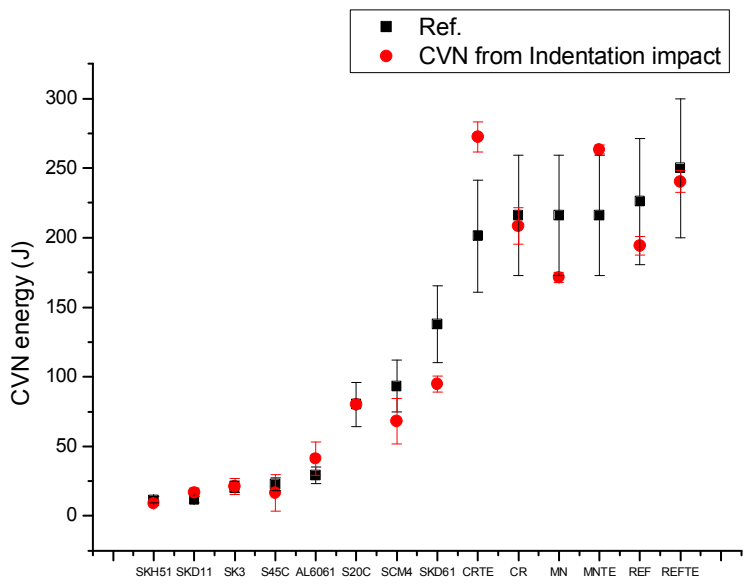
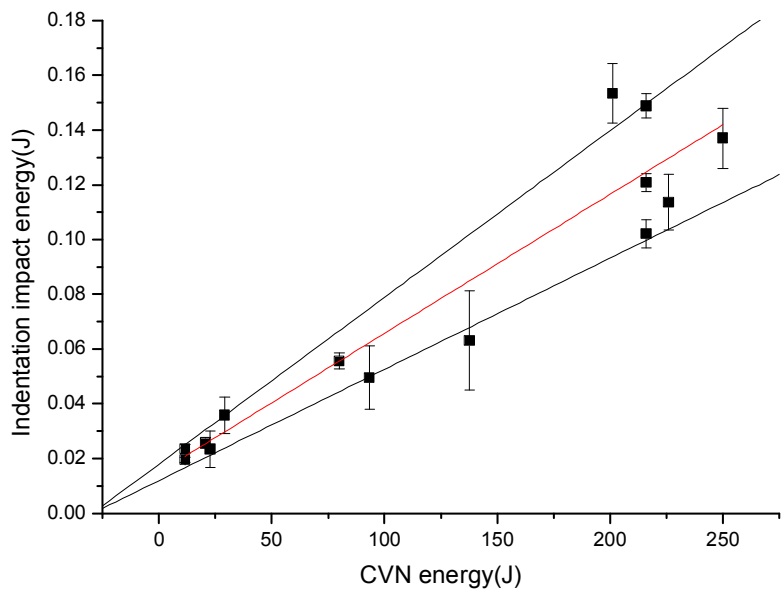


Figure 5.5. Indentation impact energy (J) vs. CVN energy (J).

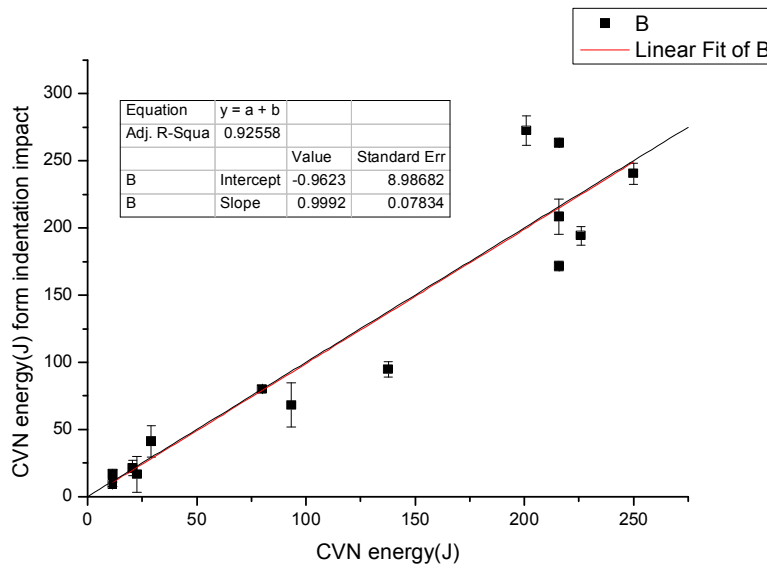


Figure 5.6. CVN energy (J) estimated from indentation impact energy vs. CVN energy (J) in reference test.

5.2.2. Model Application: Ductile-Brittle Transition Behavior

The CVN test is widely used to verify materials' ductile-to-brittle transition (DBT) behavior from the value of CVN energy in fracture behavior. Verification of DBT behavior is one of most important reliability issues in industry since brittle fracture is both instantaneous and difficult to predict. If we can predict DBT behavior by indentation impact-induced CVN energy, we would be able to use a simple method with localized testing to contribute to industrial reliability.

The CVN energy of SA508 Gr 4N, used for nuclear pressure vessels, is defined from the indentation impact energy model at various temperatures. The result is compared with the CVN test result at each temperature. As shown in Fig. 5.7, the verified CVN energy from the indentation impact energy model had transition behavior similar to the reference CVN test result. Both results showed ductile-to-brittle transition behavior at a temperature between -60 and -65°C . And the different fracture behavior of tempered SA508 Gr 4N, a transition temperature ($-40\sim-50^{\circ}\text{C}$), is also defined with indentation impact-induced CVN energy.

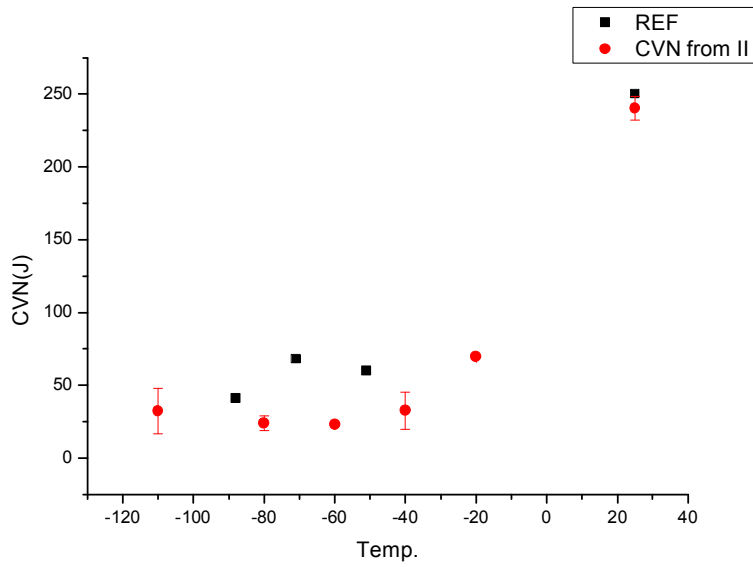
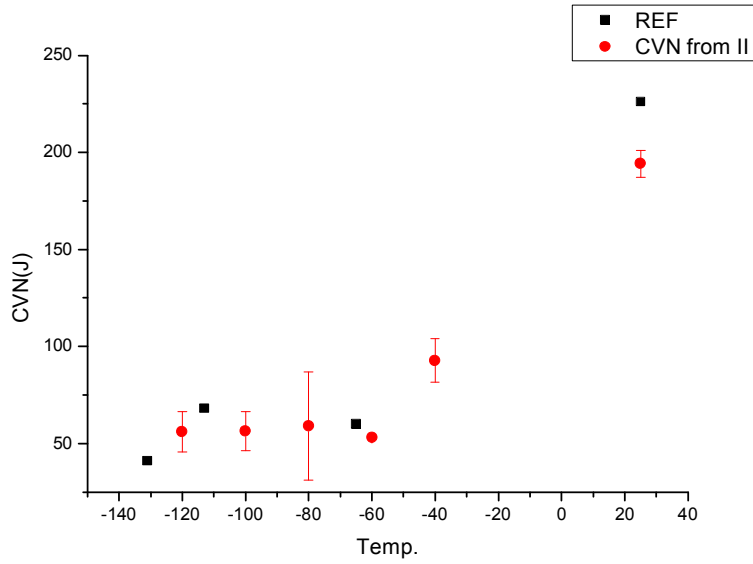


Figure 5.7. Transition behavior of (a) SA508 and (b) tempered SA508 from CVN energy change from CVN test and indentation impact test.

Chapter 6

CONCLUSIONS

The present study has proposed a model for evaluating the CVN energy of metallic materials using an indentation impact technique and an indentation impact energy model.

Indentation impact energy is defined from the indentation impact energy model with interpretations of the steps of crack formation; crack initiation, crack enlargement, and crack propagation. The indentation impact energy during each step of crack formation is derived from the criterion of indentation strain rate, which is defined from the concept of plastic zone expansion rate change during crack formation.

However, the derived energy in the final steps of crack formation (crack propagation) may contain errors, since the indentation impact test does not induce specimen failure. The end point of the test is not defined by specimen failure, as in the CVN test. Thus, the corresponding energy is complemented by relationships using similarities between CVN test and indentation impact test.

Values of CVN energy were estimated from the defined corresponding indentation impact energy for 14 different kinds of materials and were compared with the values of CVN energy measured from standard CVN tests.

1. An indentation impact energy model is defined with basic similarities between CVN test and indentation impact test. Both tests inflict dynamic fracture to materials with similar stress distribution arising from the geometrical similarities of the V notch and a sharp indenter. Using the tests similarities, CVN energy is estimated from the indentation impact energy with similar energy trends.

2. Indentation cracking is assumed to correlate an energy model with CVN energy, based on deformation induced crack formation due to reinforced strain rate effect by indentation impact test. As defined, CVN energy is the energy absorbed during impact fracture. An indentation-induced crack is generated from the nucleation of a flaw at an intercepting slip plane with maximized dislocation pile-up brought about by rapid deformation. With increasing pressure, the flaw becomes a short crack, and then propagates until the test ends. The indentation impact energy model defines the corresponding impact energy with interpretations of absorbed energy at each steps of crack formation; flaw initiation, crack enlargement, and crack propagation.

3. The criterion of indentation strain rate, defined from the concept of plastic

zone expansion rate, is used to analyze crack formation during indentation. The energy absorbed in each step of crack formation is calculated from the area of the indentation impact load-displacement curve to a critical point defined from the strain rate criterion. The energy absorbed from flaw initiation is defined by integration of the load-displacement curve to the point of maximum strain rate (h_{t1}). Because of the steady-state crack propagation of indentation, the absorbed energy of crack enlargement and propagation is classified by the constant strain rate condition (h_{t2}). The absorbed energy during crack enlargement is defined by integrating the curve between h_{t1} and h_{t2} .

4. Due to the absence of the failure end point in indentation testing, the energy absorbed during the final steps of crack formation (crack propagation) may contain errors. The corresponding energy is complemented by relationships from similarities between CVN testing and indentation impact testing. The energy absorbed during crack propagation is defined in terms of the rate of average increase in the absorbed energy during crack propagation and the correlation constants S , K and t_{pc} . These correlation constants are verified by the strain rate ratio ($\sim 10^3$) and deformed volume ratio ($\sim 1.968 \cdot 10^3$) of the indentation impact test and CVN test. t_{pc} is regarded as a

constant of ductility because it is nearly constant between materials showing the same fracture mechanism due to the extremely high CVN test velocity (3.6 ms for ductile, 1.2 ms for transition, 0 for brittle).

5. The energy absorbed in of each step of crack formation is calculated using a strain-rate criterion and complemented by definition of corresponding energy during crack propagation. As the complemented definition contains a difference in ductility, an indentation impact energy model using ductility is verified. To apply the model, ductility is predetermined by the value of absorbed energy of crack initiation (flaw initiation and crack enlargement) calculated using the concept of transition temperature.

6. To verify the proposed indentation impact energy model, CVN tests and indentation impact tests were performed for 14 different materials. The CVN energy from the indentation impact tests mostly correspond to those from the actual CVN tests. In addition, we applied this model to low-temperature testing to verify the transition behavior of SA508 and tempered SA508. The transition behavior difference between the two specimens also agreed with the indentation impact energy model.

7. Indentation impact energy model is proposed with the result of 14 selected metallic materials from developed indentation impact test device which is designed for lab scale. Application of the proposed model could be suitable for the designated test conditions; Micro Vickers indenter tip, developed device, 14 selected materials. Additional verifications on modeling parameters could be required with expansion of tested materials.

References

- [1] A.A. Griffith, Philosophical Transactions of the Royal Society, Series A **221**, 163 (1920)
- [2] G.R. Irwin, Sagamore Research Conference Proceedings **2**, 289 (1956)
- [3] ASTM Test Method E 23-02A: Standard Test Methods for Notched Bar Impact Testing of Metallic Materials (2002)
- [4] ASTM Test Method E208-95A: Standard Test Methods for Conducting Drop-Weight Test to Determine Nil-Ductility Transition Temperature of Ferritic Steels (2000)

- [5] ASTM Test Method E436-03: Standard Method for Drop-Weight Tear Tests of Ferritic Steels (2003)
- [6] ASTM Test Method E604-83: Standard Test Method for Dynamic Tear Testing of Metallic Materials (2002)
- [7] T.A. Siewert et al., A Century of Progress, ASTM 1-16 (1999)
- [8] A.E. White, Bibliography on Impact Testing (1925)
- [9] A. LeChatalier, French Testing Commission **3** (1892)
- [10] W.K. Hatt, Proceedings ASTM **2** (1902)
- [11] S.B. Russell, Transactions ASCE **39** (1898)
- [12] M.G. Charpy, Soc. Ing. Français (1901)
- [13] N.H. Fahey, Materials Research Standards **1** (1961)
- [14] D.E. Driscoll, Impact Testing, ASTM STP 176 (1955)
- [15] N.H. Fahey, Impact Testing of Metals, ASTM STP 466 (1970)
- [16] C.N. McCowan et al., Journal of Testing and Evaluation (1998)
- [17] Charpy Impact Test: Factors and Variables, ASTM STP 1072 (1990)
- [18] M.F. Doerner and W.D. Nix, J. Mater. Res. **1**, 601 (1986)
- [19] W.C. Oliver and G.M. Pharr, J. Mater. Res. **7**, 1564 (1992)
- [20] W.C. Oliver, G.M. Pharr. J. Mater. Res. **19**, 3 (2004)
- [21] D. Tabor, The Hardness of Metals, Clarendon Press (1951)
- [22] J.H. Ahn, D. Kwon, J. Mater. Res. **16**, 3170 (2001)

- [23] T.Y. Tsui, W.C. Oliver, G.M. Pharr. *J. Mater. Res.* **11**, 752 (1996)
- [24] S. Suresh, A.E. Giannakopoulos. *Acta Mater.* **46**, 5775 (1998)
- [25] A. Bolshakov, G.M. Pharr. *J. Mater. Res.* **13**, 1049 (1998)
- [26] Y.H. Lee, D. Kwon. *J. Mater. Res.* **17**, 901 (2002)
- [27] Y.H. Lee, D. Kwon. *Acta Mater.* **52**, 1555 (2004)
- [28] S. Palmquist, *Jernkontorest Ann.* **141**, 300 (1957)
- [29] B.R. Lawn, J. Wilshaw, *J. Mater. Sci.* **10**, 1049 (1975)
- [30] B.R. Lawn, M.V. Swain, *J. Mater. Sci.* **10**, 113 (1975)
- [31] B.R. Lawn, E.R. Fuller, *J. Mater. Sci.* **10**, 2016 (1975)
- [32] B.R. Lawn, A.G. Evans, D.B. Marshall, *J. Am. Ceram. Soc.* **63**, 574 (1980)
- [33] F.M. Haggag, R.K. Nanstad, *ASTM PVP* **170**, 41 (1989)
- [34] T.S. Byun, J.W. Kim, J.H. Hong, *J. Nucl. Mater.* **252**, 187 (1998)
- [35] J.B. Ju, Ph. D. thesis, Seoul National University (2003)
- [36] J.S. Lee, J.-i. Jang, B.W. Lee, Y. Choi, S.G. Lee, D. Kwon, *Acta Mater.* **54**, 1101 (2006)
- [37] A.C. Fisher-Cripps, *Introduction to Contact Mechanics*, 2nd edition (Springer, 2007)
- [38] ISO 14577-1: *Metallic Materials – Instrumented Indentation Test for Hardness and Materials Parameters – Part 1: Test Method* (2002)

- [39] ISO 14577-4: Metallic Materials – Instrumented Indentation Test for Hardness and Materials Parameters – Part 4: Test Method for Metallic and Non-metallic Coatings (2007)
- [40] ISO/TR 29381: Measurement of Mechanical Properties by an Instrumented Indentation Test – Indentation Tensile Properties (2008)
- [41] G.M. Pharr and A.J. Bolshakov, *J. Mater. Res.* **17**, 2660 (2002)
- [42] I.N. Sneddon., *Int. J. Engng. Sci.* **3**, 47 (1965)
- [43] A.E.H. Love., *Quart. J. Math.* **10**, 161 (1939)
- [44] A.E.H. Love., *Phil. Trans. A* **228**, 377 (1929)
- [45] J.W. Harding, I.N. Sneddon, *Proc. Camb. Phil. Soc.* **41**, 16 (1945)
- [46] I.N. Sneddon, *Fourier Transforms* (McGraw-Hill, New York, 1951)
- [47] Y. Liu, A.H.W. Ngan, *Scripta Mater.* **44**, 237 (2001)
- [48] J.Y. Kim, J.J. Lee, Y.H. Lee, J.I. Jang, D. Kwon, *J. Mater. Res.* **21**, 2975 (2006)
- [49] G.M. Pharr, W.C. Oliver, F.R. Brotzen, *J. Mater. Res.* **7**, 613 (1992)
- [50] C.M. Cheng, Y.T. Cheng, *Appl. Phys. Lett.* **71**, 2623 (1997)
- [51] H. Gao, T.W. Wu, *J. Mater. Res.* **8**, 3229 (1993)
- [52] E.C. Jeon, M.K. Baik, S.H. Kim, B.W. Lee, D. Kwon, *Key Eng. Mater.* **2152**, 297 (2005)
- [53] G.E. Dieter, *Mechanical Metallurgy* (McGraw-Hill, New York, 1986)

- [54] K.W. Lee, K.H. Kim, J.-Y. Kim, D. Kwon, *J. Phys. D: Appl. Phys.* **D 41**, 074014 (2008)
- [55] G.R. Antis, P. Chantikul, B.R. Lawn, D.B. Marshall, *J. Am. Ceram. Soc.* **64**, 533 (1981)
- [56] K.L. Johnson, *Contact Mechanics* (Cambridge University Press, Cambridge, 1985)
- [57] R. Hill. *The Mathematical Theory of Plasticity* (Clarendon Press, Oxford, 1950)
- [58] K.L. Johnson, *J. Mech. Phys. Sol.* **18**, 115 (1970)
- [59] K.E. Puttick, L.S.A. Smith, L.E. Miller, *J. Phys. D: Appl. Phys.* **10**, 48 (1977)
- [60] K.E. Johanns, *Modelling Simul. Mater. Sci. Eng.* **22**, 21 (2014)
- [61] S.S. Chiang, D.B. Marshall, A.G. Evans, *J. Appl. Phys.* **53**, 298 (1982)
- [62] G. Feng, S. Qu, Y. Huang, W.D. Nix, *Acta Mater* **55**, 2929 (2007)
- [63] R.F. Cook, G.M. Pharr, *J. Am. Ceram. Soc.* **73**, 787 (1990)
- [64] A.C. Bannister, British Steel PLC report **3** (1998)
- [65] J.T. Hagan, M.V. Swain, *Appl. Phys.* **11**, 2091 (1978)
- [66] B.J. Koeppel, G. Subhash, A. Chandra, *Journal of Engineering Materials and Technology.* **121**, 257 (1999)
- [67] G. Subhash et al., *J. Am. Ceram. Soc.* **91**, 2777 (2008)

- [68] R.J. Anton, G. Subhash, *Wear* **239**, 27 (2000)
- [69] H.T. Angus, *Wear* **54**, 33 (1979)
- [70] R.G. Batson, *Proc. Inst. Mech. Engrs.* **2**, 463 (1918)
- [71] C.A. Edwards, A. Herbert, *J. Inst. Metals* **25**, 175 (1921)
- [72] H.D. Espinosa et al., *Journal of Hard Materials* **3**, 285 (1992)
- [73] A.R. Fee, R. Segabache, E.L. Tobolski, *Metals Handbook* **8**, 71 (1985)
- [74] P.S. Follansbee, *J. Hardening*, 213 (1989)
- [75] B.J. Koeppel, Ph.D. Thesis, Michigan Technological University (1997)
- [76] B.J. Koeppel, G. Subhash, *Experimental Techniques* **21**, 16 (1997)
- [77] H. Kolsky, *Proc. R. Soc.* **62**, 676 (1949)
- [78] J. Lankford, *Journal of the American Ceramic Society* **64**, 33 (1981)
- [79] R. Martel, *Comm. Methodes d'Essai Mat. Constr.* **3**, 261 (1895)
- [80] H. O'Neill, Chapman & Hall (1967)
- [81] G. Ravichandran, G. Subhash, *International Journal of Solids Structures* **32**, 2627 (1995)
- [82] M.C. Shaw, *The Science of Hardness Testing and Its Research Applications*, ASM (1973)
- [83] M.C. Shaw, *Metal Cutting Principles*, Claredon Press (1984)
- [84] S. Suresh et al. *Journal of the American Ceramics Society* **73**, 2457 (1990)

- [85] K.H. Yang, A.S. Kobayashi, Proc. Conf. SEM, 41 (1989)
- [86] M. Yoshioka, Y. Naoto, Journal of Applied Physics **78**, 3431 (1995)
- [87] D. Tabor, Physical and Engineering Sciences **192**, 1029 (1948)
- [88] M.M. Chaudhri, J.K. Wells, A. Stephens, Philosophical Magazine A **43**, 643(2006)
- [89] B.D. Beake, J.F. Smith, Surface and Coating Technology **188**, 594 (2004)
- [90] B.D. Beake, S.R. Goodes, J.F. Smith, Surface and Coating Technology **187**, 17 (2001)
- [91] B.D. Beake, M.J. Ibanez, J.F. Smith, Proc. ICMCTF 2001 **398**, 438 (2001)
- [92] B.D. Beake, S.R. Goodes, J.F. Smith, R. Madani, C.A. Rego, R.I., Diamond Relat. Mater. **11**, 1606 (2002)
- [93] N.M. Jennett, J. Nunn, Philosophical Magazine **91**, 1200 (2011)
- [94] G. Belingardi, R. Vadori, International Journal of Impact Engineering **27**, 213 (2002)
- [95] T.M. Liu, W.E. Baker, Polymer Engineering and Science **31**, 753 (1991)
- [96] L. Shen, L. Wang, T. Liu, C. Ha, Macro. Mater. Eng. **291**, 1258 (2006)
- [97] M. Murakami, Melt Processed High-Temperature Superconductors, (1993)
- [98] D. François, A. Pineau, From Charpy to Presnet Impact Testing (2002)

[99] J.E. Field et al., International Journal of Impact Engineering **30**, 725 (2004)

[100] S.J. Lloyd, Proceedings of the Royal Society of London A: Mathematical, Physical and Engineering Sciences **461**, 2060 (2005)

Appendix A

DEVELOPMENT OF INDENTATION IMPACT

TEST SYSTEM

This appendix gives detailed information on the development of the indentation impact test system with solenoid actuator that is used to define the indentation impact energy model above. The indentation impact test system is designed to record the material resistance during impact deformation. Absorbed energy is defined instrumentally with the recorded material resistance. The recorded data is refined with a fitting method due to impact-test-induced oscillations.

1. Development of indentation impact test system

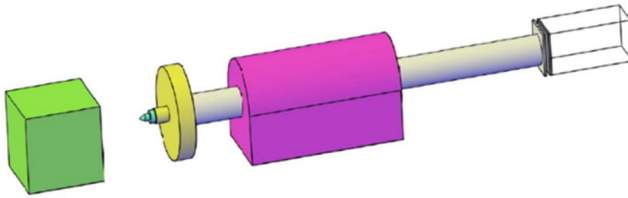
The indentation impact test system is constructed on the basis of research using the Hopkinson pressure bar [94-95]. Though pressure bar method can impart extremely high forces on the material, precise control of the testing condition is difficult with hydraulic controls. The loading mechanism of previous motor-controlled indentation devices has advantages for precise control but can provide only limited loading speeds.

We choose a different loading mechanism from previous indentation test devices, solenoid actuator, which make possible instantaneous high force applied and controlled through brief test periods. A solenoid actuator (see the detailed information in Fig. A.2) developed by KENDRION was installed in the device. As the device is loaded in a few dozen micro-seconds, sensing

devices to record the response must be selected carefully. A displacement sensor based on laser sensing is used because of its non-contact sensing and also because it offers the necessary high resolution during the impact period. A laser displacement sensor by Panasonic, HL-C201A (detailed information in Fig. A.3) is installed in the device. A dynamic load cell by CURIO TEC is applied to the loading sensor. An S-type load cell model of dynamic load cell (see Fig. A.4) is installed in the device. Figure A.5 shows the complete indentation impact test system.

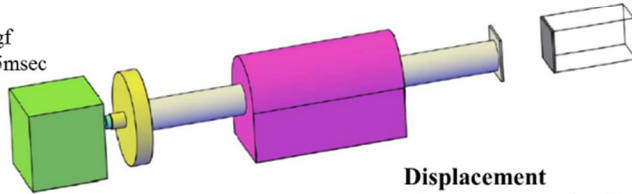
Velocity

$V = 1\sim 10\text{m/s} \sim \text{solenoid power (1}\sim 10\text{N, for Indenter+axis weight = 1kg,)}$



Load

- Load cell use 5~10kgf
- good resolution in 15msec



Displacement

- Laser sensor sensing displacement 15mm
- good resolution in 15msec

Safety

- safety design of device & indenter

Figure A.1. Basic concept of indentation impact test system.



Technische Daten LHS0600008	
Zeichnungsnummer	LHS060000A00
Zeichnungsnummer alt	GHB6082.01.A0103
Spannung [V]	24
Einschaltdauer [%]	100
Hub [mm]	12
Kraft [N]	35
Stromaufnahme [A]	1,08
Schutzart Gerät (IP)	54

(KENDRION, Germany)
LHS060 stroke = 12mm, force = 155N(15.8kgf 5%)

Figure A.2. Solenoid actuator (LH0600008).



	Panasonic
Model	HL-C201A
Beam source	Red semiconductor laser class 1 (Emission peak wavelength: 658nm)
Measurement center distance	10 ± 1 mm
Resolution	0.04 μm

Figure A.3. Laser displacement sensor (HL-C201A).



	CURIO TEC
Model	CSBA
R.C	100 kgf
R.O.	3.0mV/V ± 0.03%
Combined error	0.03%
Repeatability	0.01%
Creep	0.03 % in 30min
Zero balance	0.0 ± 0.1mV/V

Figure A.4. Dynamic load cell (CSBA).

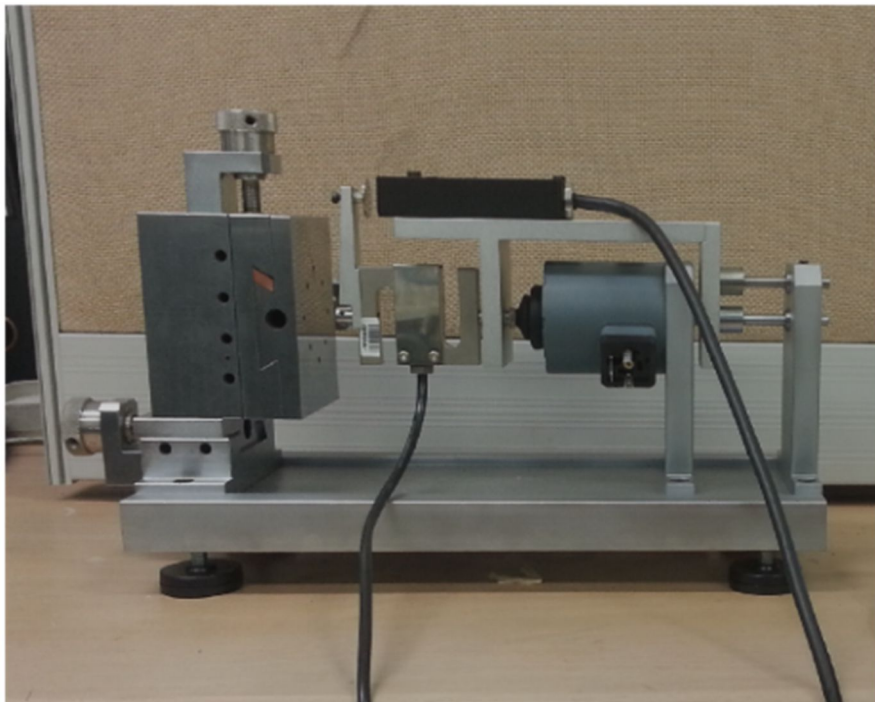
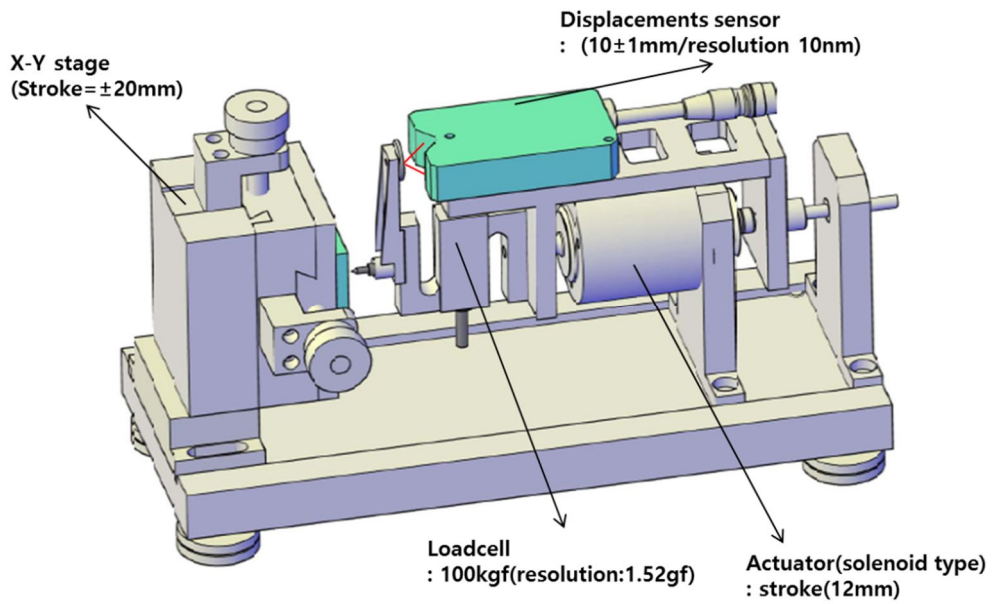


Figure A.5. Indentation impact test system.

2. Interpretation of indentation impact results

Because of the high sensor resolution, massive amounts of raw data were recorded during the short impact time. Thus the recorded data contains much scatter induced by oscillation of the device, as shown in Fig. A.6. Since observation of the suggested fracture criterion for indentation impact energy model needs clear indentation curve slope, the scatter must be reduced.

Because of the overall shape of the load and displacement versus time, logistic curve fitting is selected. Figure A.7 is the logistic curve fit result of the load versus time curve. The compatibility of the curve can be defined with the R-square method. Compatibility is regarded as good if the R value is close to 1; the R value in Fig. A.7 was 0.99.

$$y = \frac{A_1 - A_2}{1 + (x / x_0)^p} + A_2 \quad (\text{A-1})$$

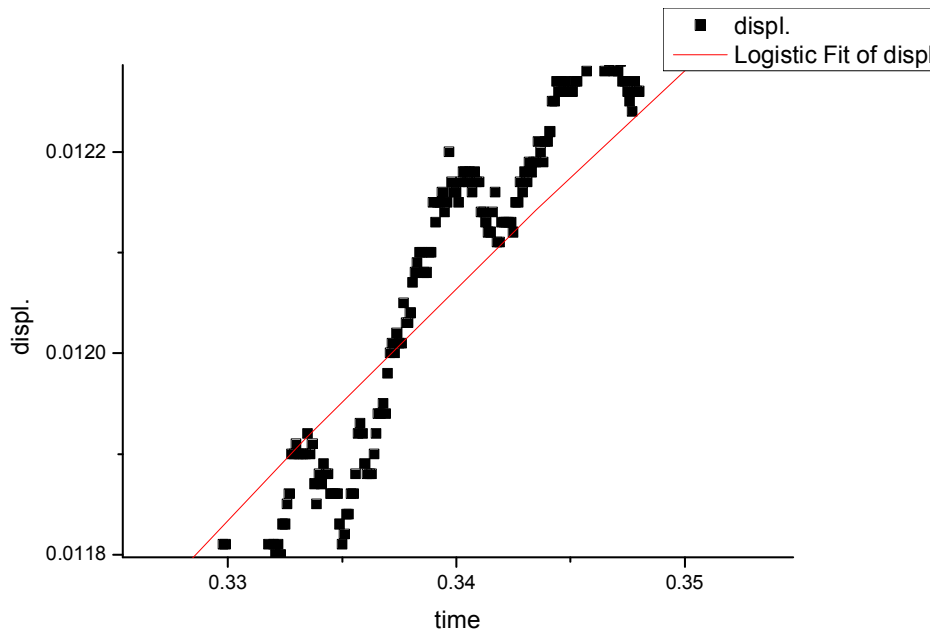


Figure A.6. Raw data for impact displacement vs. time.

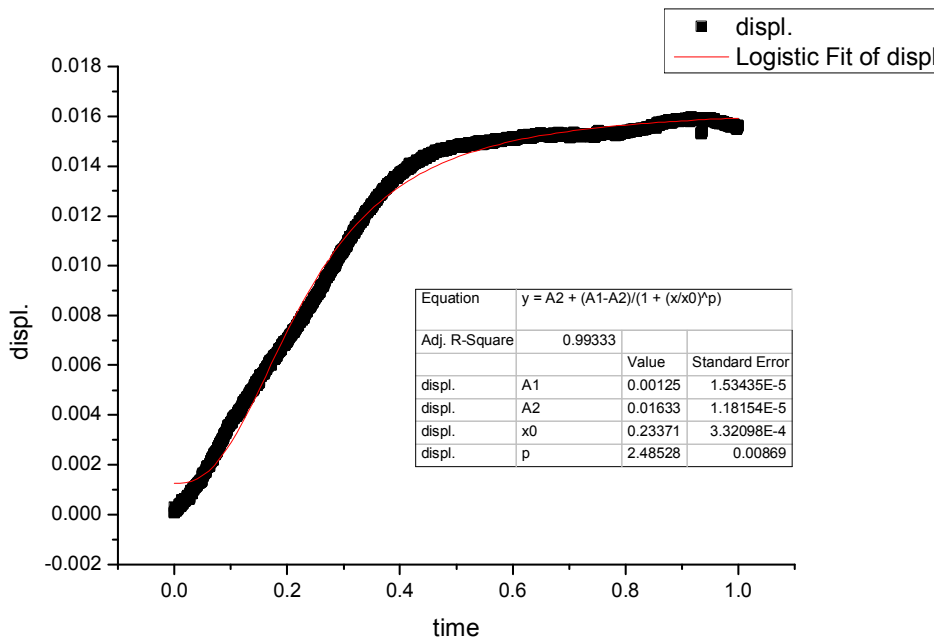


Figure A.7. Logistic curve fitting of indentation impact load vs. time curve.

초 록

재료의 미세한 파손은 광범위한 손상으로 이어져 전체 구조물의 고장을 유발할 수 있기에 구조 재료의 신뢰성 평가는 구조물의 안전에 있어서 매우 중요하다. 특히 원자력 발전 설비 등의 발전과 관련한 거대한 산업시설의 경우 고온, 고압 등의 극한 환경에서 가동되는 설비들을 많이 함유하고 있어 재료의 파손에 상대적으로 취약한 환경에 노출되어 있으며 파손이 발생하였을 때 그 피해가 단순 큰 경제적 손실을 야기할 뿐 아니라, 사회적 안전에 큰 문제를 야기할 수 있기 때문에 신뢰성 평가에 대한 중요성이 많이 인식되고 있다. 하지만 기존의 보편적인 재료시험법의 경우, 실제 가동환경(in-field)에서 평가하는데 여러 한계를 가지고 있어 그 보완에 대한 요구가 계속적으로 이루어지고 있는 상황이다.

원자력 발전설비의 경우, 중성자 취화 등에 의하여 재료의 파괴가 일어날 수 있어 일반적으로 샤르피 충격시험법을 활용하여 파괴특성을 예측하고 있다. 샤르피 충격시험법은 표준화 되어 있는 시험법으로 간단하고 쉬운 시험법이나, 기본적으로 파괴를 수반하며 일정 크기 이상의 시험편을 요구하기 때문에 가동환경에서의 평가에

한계를 지니고 있다.

이에 시험편 크기에 제한이 없고, 국부 물성평가가 가능하여 가동 환경 평가에 적합한 장점을 가지고 있는 계장화압입시험법이 그 대안으로 제안되고 있다. 많은 연구자들이 이러한 계장화 압입시험법의 장점을 기반으로 압입시험법을 파괴특성평가에 응용하기 위한 시도를 하였다. 하지만 보편적으로 활용되는 샤르피 충격시험을 기반으로한 파괴특성은 동적변형상황에서의 특성으로 일반적으로 정적변형으로 알려져있는 압입시험법을 응용하기에는 여러 한계가 존재하며 추가적으로 고려해야할 요소들이 존재하였다. 본 연구에서는 압입시험법을 동적변형상황까지 확장시킨 ‘압입충격시험법’을 활용하여 기존의 한계에대한 솔루션을 제시하였으며, 압입충격에너지모델을 제안하여 압입충격파괴 상황에서의 흡수에너지를 측정하여 에너지로 표현되는 샤르피 충격시험 결과와 연결시켜 설명하였다. 압입충격에너지는 두 시험법간의 유사성(기하학적, 응력분포, 균열양상)을 기반으로 제안되었으며, 균열 생성에 따른 소성역성장 속도 변화와 압입 변형률속도의 정의로부터 얻어진 변형률속도 기반의 criterion으로 균열 형성 단계(flaw initiation, crack enlargement, crack propagation)에 따라 구분하여 해석하였다. 15종의 다양한 금속

소재에 대하여 압입충격에너지를 평가하였으며, 표준 샤르피 충격 시험법을 기반으로 검증하였다. 그 결과 $\pm 20\%$ 오차범위에서 실제 충격시험에너지의 경향과 일치하는 것을 확인할 수 있었다.

위의 결과를 통하여 압입충격시험법이 가동 중 구조물의 열화에 따른 충격파괴특성 변화를 평가 가능한 효율적인 시험법임을 확인할 수 있다. 또한, 본 시험법의 뛰어난 가동환경 평가에 대한 적용성을 기반으로 표준 시험법인 샤르피 시험법의 대체 시험법으로써 제안이 될 수 있을 것으로 기대된다.

주요어: 압입충격시험, 샤르피 충격에너지, 압입 균열 형성, 변형률 속도 해석

학번: 2009-20639

List of Publications

I. International Journal

Won Je Jo, Hee-Jun Ahn, Jong Hyoung Kim, Dongil Kwon, Study on the fracture characteristics of frit bonding through in-situ nano-indentation testing. Journal of materials science & technology, (2015) (Accepted)

II. Korean Journal

조현욱, 도정현, 조원제, 정현득, 이재현, 조창용, 고크롬 백주철의 미세조직과 기계적 특성에 미치는 초기응고 조직의 영향, 한국주조 공학회지, 35, 6, 2015

III. International Conference (* indicates speaker)

Won Je Jo, Chan-Pyoung Park*, Seung-Kyun Kang, Dongil Kwon, Using instrumented indentation to evaluate high-temperature mechanical properties, ISOPE-2010

Won Je Jo, Won-Seok Song, Yong-Cheon Kim*, Dongil Kwon, In Service Inspection and Safety Assessment of Industrial Facilities Using Instrumented Indentation Technique, ISOPE-2011

Won Je Jo, Chan-Pyoung Park, Kug-Hwan Kim, Seung-Kyun Kang, Dongil Kwon, Instrumented Indentation Testing to Evaluate High-Temperature Material Properties, ASME 2011 Pressure Vessels & Piping Conference

IV. Korean Conference (* indicates speaker)

김국환, 박찬평, 조원제, 권동일, 계장화 압입시험법을 이용한 Ti-6Al-4V 합금의 고온 변형 거동 해석, 2010년도 대한금속재료학회 춘계 학술대회

박찬평, 강승균, 조원제, 권동일, 계장화 압입 시험을 이용한 고온 구조물 신뢰성 평가, 2010년도 한국신뢰성 학회 춘계 학술대회

강승균, 김영천, 조원제, 권동일, 연속압입시험을 이용한 발전설비 용접부의 강도 프로파일링 평가, 2010년도 대한금속재료학회 추계 학술대회

조원제, 이규제, 이진우, 권동일, In-situ SEM indentation 을 이용한 Glass Frit material의 기계적 특성 예측 연구, 2012년도 대한금속재료

학술대회 춘계 학술대회

이진우, 김준영, 조원제, 전승원, 권동일, 연속압입시험법을 이용한
금속재료의 샤르피 충격에너지 예측, 2012년도 대한금속재료학회
춘계 학술대회

이진우, 조원제, 권동일, 연속압입시험을 활용한 OLED 패널의 접합
부 충격특성 평가, 2014년도 대한금속재료학회 춘계 학술대회